



HOST UNIVERSITY: The University of Edinburgh  
FACULTY: School of Engineering  
DEPARTMENT: Civil and Environmental Engineering  
Academic Year 2017-2018

**IGNITION OF POLYMERS UNDER TRANSIENT HEATING**

Júlia Coelho Trojan

Promoters:

Dr. Rory Hadden

Dr. Ricky Carvel

Master Thesis submitted in the Erasmus+ Study Program  
**International Master of Science in Fire Safety Engineering**

## **DISCLAIMER**

This thesis is submitted in partial fulfillment of the requirements for the degree of The International Master of Science in Fire Safety Engineering (IMFSE). This thesis has never been submitted for any degree or examination to any other University/programme. The author(s) declare(s) that this thesis is original work except where stated. This declaration constitutes an assertion that full and accurate references and citations have been included for all material, directly included and indirectly contributing to the thesis. The author(s) gives (give) permission to make this master thesis available for consultation and to copy parts of this master thesis for personal use. In the case of any other use, the limitations of the copyright have to be respected, in particular with regard to the obligation to state expressly the source when quoting results from this master thesis. The thesis supervisor must be informed when data or results are used.

Júlia Coelho Trojan

A handwritten signature in black ink that reads "Júlia Coelho Trojan". The signature is written in a cursive style with a small pink square mark at the end of the word "Trojan".

Read and approved

30/04/2018

Word count: 11,433

## **ABSTRACT (English)**

Ignition is a key parameter for fire risk assessment, since it governs the flame spread and, therefore, the fire growth. In the present work, an experimental study on PMMA samples exposed to transient heating is performed, which is a more realistic approach in comparison to real fires. The aim of this thesis is to understand the parameters involved in the ignition of solids and how these parameters vary with different heating rates. In order to do so, black PMMA samples measuring 85 x 85 x 25 mm were exposed to three different linear heating rates - 40, 60 and 80 W/m<sup>2</sup>.s - in the Fire Propagation Apparatus (FPA). The parameters compared were critical mass loss rate, critical surface temperature, ignition delay time, incident heat flux at ignition and surface losses. Also, experiments using constant incident heat fluxes were also performed in order to compare with the literature. The mass loss rate was found to increase with the heating rate, and this trend is reported in previous works. However, the deviation between the experiments was significantly high. The average values were 3.69, 3.83 and 4.06 g/m<sup>2</sup>.s for the heating rates of 40, 60 and 80 W/m<sup>2</sup>.s, respectively. The maximum value was 5.73 g/m<sup>2</sup>.s, whereas the minimum was 2.73 g/m<sup>2</sup>.s, both at a heating rate of 80 W/m<sup>2</sup>.s. The critical surface temperature was observed to increase with the heating rate, which is in accordance with previous works. However, the temperatures were quantitatively lower than the ones reported in the literature. The maximum value for surface temperature was 303.94°C at the heating rate of 80 W/m<sup>2</sup>.s, whereas the minimum was 226.91°C at the heating rate of 40 W/m<sup>2</sup>.s. Ignition delay times decreased with the heating rate, whereas the incident heat flux at ignition increased. The net heat flux and the surface losses were found to increase with the heating rate, and an average value of 6 kW/m<sup>2</sup> was found for the former and 31.75 kW/m<sup>2</sup> for the latter.

## RESUMO (Portuguese)

Ignição é um parâmetro fundamental na avaliação de risco de incêndio, já que é o responsável pela propagação de chamas e, conseqüentemente, para propagação de incêndios. No presente trabalho, um estudo experimental foi realizado utilizando amostras de PMMA expostas a regime transiente de transferência de calor, que é uma condição mais realista em incêndios reais. O objetivo dessa dissertação é entender os parâmetros envolvidos na ignição de sólidos e como esses parâmetros variam com diferentes taxas de aquecimento. Para tal, amostras de PMMA medindo 85 x 85 x 25 mm foram expostas a três diferentes taxas lineares de aquecimento – 40, 60 e 80 W/m<sup>2</sup>.s – no Fire Propagation Apparatus (FPA). Os parâmetros comparados foram taxa crítica de perda de massa, temperatura crítica da superfície, retardo de ignição, fluxo de calor incidente no momento da ignição e perdas de calor pela superfície. Visando a comparar com literatura, experimentos com fluxo de calor constante foram realizados. Foi observado que a taxa de perda de massa diminuiu com o aumento na taxa de aquecimento, e essa mesma tendência foi relatada na literatura. Entretanto, o desvio entre os resultados obtidos foi significativamente alto. Os valores médios encontrados foram 3.69, 3.83 e 4.06 g/m<sup>2</sup>.s para as taxas de aquecimento de 40, 60 e 80 W/m<sup>2</sup>.s, respectivamente. O maior valor observado foi 5.73 g/m<sup>2</sup>.s, enquanto que o menor foi 2.73 g/m<sup>2</sup>.s, ambos na taxa de aquecimento de 80 W/m<sup>2</sup>.s. A temperatura crítica da superfície aumentou com a taxa de aquecimento, e este resultado está de acordo com a literatura. Entretanto, as temperaturas observadas são quantitativamente mais baixas do que as observadas na literatura. A temperatura máxima obtida foi 303.94°C na taxa de aquecimento de 80 W/m<sup>2</sup>.s, enquanto que a menor foi 226.91°C na taxa de aquecimento de 40 W/m<sup>2</sup>.s. O tempo de retardo de ignição diminuiu com a taxa de aquecimento, enquanto que o fluxo de calor incidente no momento da ignição aumentou. O fluxo de calor líquido e as perdas de calor na superfície aumentaram com a taxa de aquecimento, e um valor médio de 6 kW/m<sup>2</sup> foi observado para o primeiro e de 31.75 kW/m<sup>2</sup> para o último.

# List of contents

DISCLAIMER.....	ii
ABSTRACT (English) .....	iii
RESUMO (Portuguese) .....	iv
List of Figures .....	vii
List of Tables .....	ix
Notation.....	1
CHAPTER 1.....	3
INTRODUCTION.....	3
1.1. Motivation.....	4
1.2. Objectives .....	4
1.3. LITERATURE REVIEW .....	5
1.3.1. The ignition process .....	5
1.3.1.1. The solid phase: Pyrolysis process.....	5
1.3.1.2. The gas phase .....	7
1.3.2. Heat transfer process.....	9
1.3.3. Mass transfer process .....	11
1.3.4. The classic ignition theory.....	12
1.3.5. PMMA.....	15
1.3.6. Previous works .....	15
CHAPTER 2.....	23
METHODOLOGY.....	23
2.1. Samples preparation.....	23
2.2. The Fire Propagation Apparatus (FPA) .....	26
2.3. Description of the experiments .....	27
2.4. Mass Loss Rate (MLR) measurements .....	29
2.5. Temperature.....	31
2.5.1. Surface temperature .....	32
2.5.2. Heat losses .....	32
2.6. Propagation of uncertainties .....	33
CHAPTER 3.....	35
RESULTS AND DISCUSSION .....	35
3.1. MLR experiments.....	35

3.1.1.	Transient heating .....	35
3.1.2.	Constant heating .....	38
3.2.	Temperature Experiments.....	39
3.2.1.	Temperature distribution within the solid fuel.....	40
3.2.2.	Transient heating .....	41
3.2.3.	Constant heating .....	44
3.2.4.	Conductive heat losses.....	45
3.2.5.	Radiative and convective heat losses .....	48
3.2.6.	Net heat flux (NHF).....	49
3.3.	Incident heat flux at ignition and ignition delay time.....	50
3.4.	Bubble formation.....	53
3.5.	Limitations and source of errors.....	55
CHAPTER 4.....		59
CONCLUSION.....		59
4.1.	Recommendation for future work.....	60
ACKNOWLEDGMENTS .....		61
REFERENCES .....		62
Appendix I .....		64
Appendix II.....		68

## List of Figures

Figure 1 – Schematic of the degradation process that a solid undergoes prior to ignition [3].	5
Figure 2 – Pyrolysis and ignition times plotted as a function of different heat fluxes [8].	7
Figure 3 – Increase in the surface temperature of a solid with time and the different steps that are undergone by the solid fuel [9].	9
Figure 4 – Heat transfer mechanisms in a control volume for $x < \epsilon_p$ [3].	10
Figure 5 – Cross-sections of acrylic samples subject to different incident heat fluxes and their respective ignition delay time ( $t_{ig}$ ). [13].	12
Figure 6 – Ignition delay time as a function of the incident heat flux for PMMA. Extracted from Chapter 21 of the SFPE Handbook of Fire Protection Engineering [3].	14
Figure 7 – Time to ignition and IHF at ignition as a function of the heating rate [10].	16
Figure 8 – Mass loss rate per unit area as a function of the heating rate [10].	17
Figure 9 – Ignition delay time as a function of the incident heat flux for black PMMA. Data extracted from Rhodes [17].	19
Figure 10 – Critical mass flux for different incident heat fluxes at (a) flash point and (b) fire point [18].	20
Figure 11 – Comparison between results from previous works for critical mass flux. Extracted from [7].	21
Figure 12 – Front (left-hand side) and back (right-hand side) surfaces of the samples for mass experiments.	23
Figure 13 – Sample used for temperature experiments.	24
Figure 14 – Schematic of the thermocouple position in the sample.	24
Figure 15 – Schematic of the Fire Propagation Apparatus (FPA). Extracted from Chapter 36 of the SFPE Handbook [3].	27
Figure 16 – Experimental set-up for mass loss experiments in the Fire Propagation Apparatus.	28
Figure 17 – Experimental set-up for temperature experiments in the Fire Propagation Apparatus.	29
Figure 18 – Graphs plotted from sample T-40-2-M illustrating the methodology used for the MLR calculation; a) Mass as function of time for the whole experiment and b) Zoom from a) showing the mass per unit area plotted against time and the linear fit according to visual analysis.	30
Figure 19 – Detail on the thermocouples position at 4, 12 mm and in the aluminium block.	31
Figure 20 – Top view from the experimental set-up for temperature experiments.	32
Figure 21 – Temperature vs. Time for the aluminium block temperature. Sample T-80-2-T (subjected to a heating rate of $80 \text{ W/m}^2\cdot\text{s}$ )	34
Figure 22 – Mass loss rate per unit area calculated based on a visual analysis.	35
Figure 23 – Mass loss rate per unit area calculated based on the last 10s.	36
Figure 24 – Average MLR per unit area for the visual analysis as a function of the incident heat flux.	38
Figure 25 - Average MLR per unit area for the last 10 seconds as a function of the incident heat flux.	39
Figure 26 – Temperature distribution with depth in the sample T-60-1-T.	40

Figure 27 – Temperature evolution with time at all depths studied (4, 8, 12 and 16 mm). Sample T-60-1-T.....	40
Figure 28 – Surface temperature as a function of the heating rate. ....	41
Figure 29 – Temperature at the depths of 4, 8, 12 and 16 mm as a function of the heating rate.....	42
Figure 30 – Surface temperature as a function of the incident heat flux.....	44
Figure 31 – Temperatures at 4 and 8 mm as a function of the incident heat flux. ....	44
Figure 32 – Temperature evolution with time at different depths for a PMMA sample subjected to a constant incident heat flux of 50 kW/m <sup>2</sup> . ....	45
Figure 33 – Average of the conductive heat losses as a function of the heating rate for the transient heating case.....	46
Figure 34 – Average of the conductive heat losses as a function of the incident heat flux for the constant heating case. ....	46
Figure 35 – Temperature variation with time in the aluminium block for samples a) T- 40-3-T and b) T-40-1-T.....	47
Figure 36 – Radiative and convective heat losses at the exposed surface as a function of the heating rate.....	48
Figure 37 - Radiative and convective heat losses at the exposed surface as a function of the incident heat flux. ....	49
Figure 38 – Net heat flux as a function of the heating rate for the experiments under transient irradiation.....	50
Figure 39 – Time to ignition and incident heat flux at ignition for the three different heating rates.....	51
Figure 40 – Time to ignition vs. Heating rate for the present work and value from literature [5].....	52
Figure 41 – Time to ignition as a function of the incident heat flux for the constant heating case. ....	52
Figure 42 – Ignition delay time as a function of the IHF for the present work and results obtained by Rhodes [16].....	53
Figure 43 – Bubbling formation in a PMMA sample subjected to a heating rate of 40 W/m <sup>2</sup> .s.....	54
Figure 44 - Bubbling formation in a PMMA sample subjected to a heating rate of 60 W/m <sup>2</sup> .s.....	54
Figure 45 - Bubbling formation in a PMMA sample subjected to a heating rate of 80 W/m <sup>2</sup> .s.....	54



## List of Tables

Table 1 – Summary of parameters involved in the pyrolysis process and their respective description. Extracted from Chapter 21 of the SFPE Handbook of Fire Protection Engineering [3].	6
Table 2 – Summary of the parameters involved in the heat transfer for $x < \epsilon_p$ and their respective description [3].	10
Table 3 – Ignition delay time for different heating rates. Extracted from [5].	16
Table 4 – Summary of ignition conditions reported by Vermesi <i>et al.</i> for different scenarios. Data extracted from [6].	17
Table 5 – Results obtained by Lyon <i>et al.</i> for different parameters at ignition by looking at the solid phase [15].	18
Table 6 – Results obtained by Lyon <i>et al.</i> for different parameters at ignition by looking at the gas phase [15].	18
Table 7 – Ignition delay times and ignition temperature for black PMMA for the heat fluxes 19 and 50 kW/m <sup>2</sup> obtained by Rhodes [16].	19
Table 8 – Sample identification for the mass loss experiments under transient conditions.	25
Table 9 - Sample identification for the mass loss experiments under constant incident heat flux.	25
Table 10 - Sample identification for the temperature experiments under transient conditions.	26
Table 11 - Sample identification for the temperature experiments under constant incident heat flux.	26
Table 12 – Summary of results for MLR based on the visual analysis and last 10 seconds intervals.	36
Table 13 – Comparison between the values from literature and the ones obtained in the present work.	37
Table 14 – Summary of the results obtained for MLRPUA for the visual analysis and last 10 seconds for the samples subjected to constant incident heat flux.	39
Table 15 – Summarized results of average surface temperature and the difference between the maximum and minimum values obtained (Error + and Error -, respectively).	41
Table 16 – Summary of surface temperature results from literature and present work.	43
Table 17 – Comparison of the results obtained in the present work and previous works.	45
Table 18 – Conductive heat losses and the respective uncertainty for each experiment.	48
Table 19 – Comparison between results obtained by Rhodes [16] and the present work.	53

## Notation

$A$  – surface area [ $\text{m}^2$ ]

$c$  – specific heat [ $\text{kJ}/\text{kg.K}$ ]

FPA – Fire Propagation Apparatus

HR – heating rate

IHF – incident heat flux

$k$  – thermal conductivity [ $\text{W}/\text{m.K}$ ]

$m$  – mass [ $\text{g}$ ]

$\dot{m}''_{ig}$  – critical mass loss rate [ $\text{g}/\text{m}^2.\text{s}$ ]

MLR – mass loss rate

MLRPUA – mass loss rate per unit area [ $\text{g}/\text{m}^2.\text{s}$ ]

MPUA – mass per unit area [ $\text{g}/\text{m}^2$ ]

NHF – net heat flux [ $\text{kW}/\text{m}^2$ ]

$\dot{q}_{cond}$  – conductive heat losses to the aluminium block [ $\text{kW}/\text{m}^2$ ]

$\dot{q}_{loss}$  – radiative and convective heat losses [ $\text{kW}/\text{m}^2$ ]

$\dot{q}''_{net}$  – net heat flux [ $\text{kW}/\text{m}^2$ ]

$t_{ig}$  – time to ignition or ignition delay time [ $\text{s}$ ]

$T_{ig}$  – critical surface temperature [ $^{\circ}\text{C}$ ]

VA – visual analysis of the mass loss



## CHAPTER 1

### INTRODUCTION

A great obstacle in the field of fire safety is the accurate prediction of the growth and spread of a fire. The first step in fire simulation is to determine the fuel load in a certain compartment. Once it is determined, the fire spread and growth are described ideally by means of the material properties and configuration of the compartment. According to Tewarson *et al.*, fire hazards can be classified in thermal or nonthermal. The former regards the damage caused by the excessive heat generated by the fire, whereas the latter is related to the release of toxic chemical compounds [1].

Fire behaviour is described in terms of the following parameters [1]:

- Ignition;
- Flame spread;
- Peak burning or steady combustion;
- Heat generation;
- Hazardous chemical compounds generation;
- Flame extinction.

The present work is focused on the first parameter by understanding the ignition phenomenon under more realistic scenarios.

In fire simulations, ignition can be modelled either by pyrolysis modelling or by describing ignition criteria, i.e. using as input the critical surface temperature

The search for new materials that are lightweight, low cost and present better mechanical performance led to the development of composite materials. An example of the industrial applicability of such materials is the Airbus 380, which has more than 50% of its structures made of composite materials. The main problem associated to this type of materials concern their behaviour under fire conditions [2]. When heated, polymeric materials undergo *thermal decomposition* and *thermal degradation*. The former is defined as “a process of extensive chemical species change caused by heat”, whereas the latter as “a process whereby the action of heat or elevated temperature on a material, product or assembly causes a loss of physical, mechanical or electrical properties” [3].

## **1.1. Motivation**

In the field of fire safety engineering, the performance-based design approach is the most utilized. A very important engineering tool is fire simulation, and it is performed in order to prove that the solution presented is at least as safe as commonly accepted solutions [2]. Therefore, it is of great importance to ensure the quality of computational simulations.

As aforementioned, the accurate determination of fire risk is highly related to flame spread prediction. In order to accurately model the propagation of a fire, pyrolysis and ignition parameters must be properly described. An extensive literature is available (see 1.3.6) on the burning behaviour of polymers. However, they mostly utilize constant incident heat fluxes. Furthermore, the current ignition criteria is based on constant incident heat fluxes (IHF), which is not representative for a realistic fire, where the fire growth leads to a constant increase in the incident heat flux to unburned materials. Therefore, a transient analysis is a more suitable option to represent this scenario.

The material used in the present work is poly(methyl)methacrylate. It is a widely used material in a broad variety of applications, such as furniture, electrical appliances, glazing, panels, screens, and so on [4]. Moreover, a vast literature is available on the burning behaviour of PMMA (see 1.3.6), and therefore more information is available to compare to the results obtained in the present work.

## **1.2. Objectives**

The aim of the present work is, therefore, to assess the ignition of poly(methyl)methacrylate under transient conditions.

Considering that the current ignition criterion is based on critical mass flux and critical surface temperature, these parameters are studied here. The main goal is to observe possible trend in these parameters and in the heat flux at ignition and ignition delay time. Moreover, the heat losses are also assessed in order to understand the heat balance within the solid material at ignition.

### 1.3. LITERATURE REVIEW

#### 1.3.1. The ignition process

Ignition is defined as the initiation of flaming combustion [3].

When a solid material is subjected to external heating, it undergoes several physical and chemical processes of degradation. These processes may lead to flaming ignition, which is controlled by the heating and pyrolysis of the solid fuel and the gas-phase chemical reactions. Therefore, the ignition process can be assessed in terms of the solid or the gas phase [3, 5]. These phases will be explained separately below.

##### 1.3.1.1. The solid phase: Pyrolysis process

Pyrolysis is the process of thermal degradation that solid materials undergo prior to ignition [2]. This process leads to the formation of gaseous fuel and tends to be an endothermic process of molecules breakdown [3,7]. Figure 1 illustrates the several processes undergone by a solid material, whereas Table 1 presents the variables involved in the process.

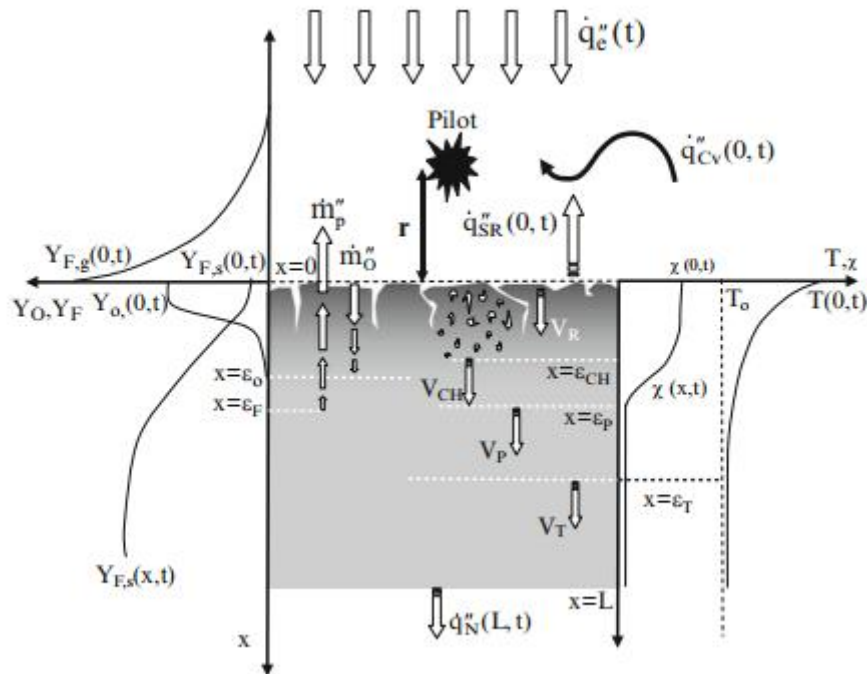


Figure 1 – Schematic of the degradation process that a solid undergoes prior to ignition. Extracted from Chapter 21 [3].

Table 1 – Summary of parameters involved in the pyrolysis process and their respective description.

Extracted from Chapter 21 of the SFPE Handbook of Fire Protection Engineering [3].

<b>Parameter</b>	<b>Description</b>
$\dot{m}''_O$	Mass flux of oxidizer
$\dot{m}''_P$	Production of gas phase fuel per unit area
$\dot{q}''_{Cv}$	Convective losses from the surface
$\dot{q}''_e(t)$	External radiative heat flux
$\dot{q}''_N$	Heat losses through the back-face of the material
$\dot{q}''_{SR}$	Radiation from the exposed surface to the surrounding
$T_0$	Ambient temperature
$T(x, t)$	Temperature as a function of depth and time
$V_{CH}$	Propagation velocity of the charring depth ( $\epsilon_{CH}$ )
$V_R$	Surface regression rate
$V_P$	Propagation velocity of the pyrolysis depth ( $\epsilon_P$ )
$V_T$	Thermal wave velocity
$Y_O(x,t)$	Local oxygen concentration
$Y_{F,g}(x, t)$	Fuel concentration external to the sample
$Y_{F,s}(x, t)$	Mass fraction of flammable gases in the local products of degradation
$\epsilon_O(t)$	Depth of the region where oxygen is present in relevant quantities (Oxygen penetration depth)
$\epsilon_{CH}$	Charring depth
$\epsilon_F(t)$	Depth of the region where fuel is being produced (Reactive depth)
$\epsilon_P$	Pyrolysis depth
$\epsilon_T$	Thermal depth
$\chi(x, t)$	Fuel permeability function

The time to ignition ( $t_{ign}$ ) is divided into three different steps, namely the pyrolysis time ( $t_p$ ), the mixing time ( $t_{mix}$ , also called transport and diffusion time) and the chemical induction time ( $t_{chem}$ ). However, the pyrolysis time is much larger than the mixing and chemical times, and therefore the assumption  $t_{ign} = t_p$  is generally adopted [7]. Nevertheless, recent studies carried out by Dakka *et al.* have shown that the mixing time cannot be neglected. As showed in Fig. 2, there is a discrepancy between pyrolysis time and ignition time, which suggests that the mixing time is relevant [8]. Moreover, this result also shows that the assumption that the material remains inert until ignition is questionable [3].

Nonetheless, in the present work mixing and induction time are neglected. This assumption can be made due to the fact that a pilot flame is used. This will be further clarified in 1.3.1.2. Moreover, all the parameters studied here are related to the solid phase.

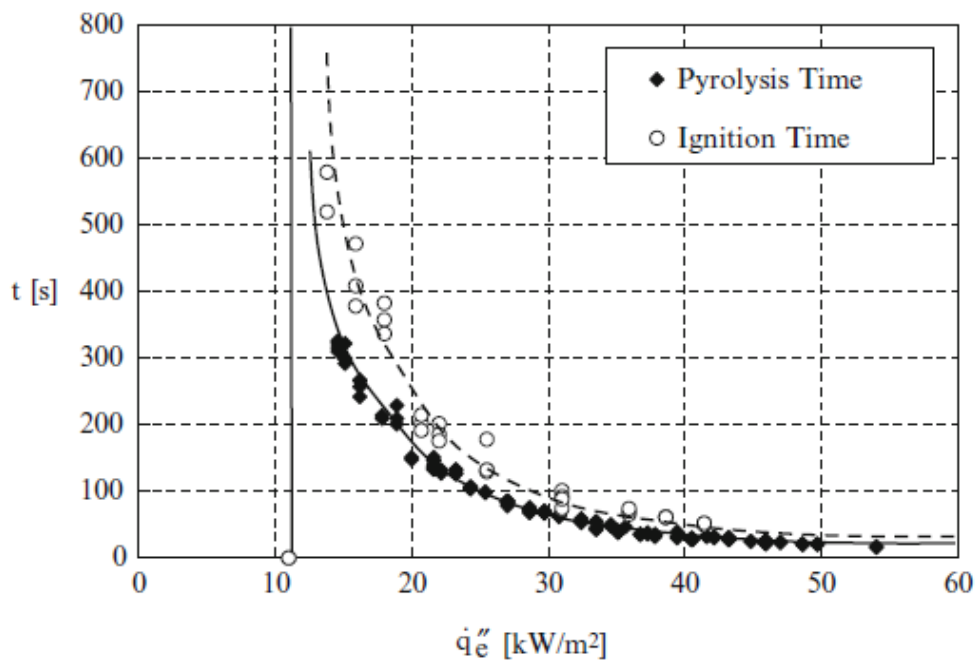


Figure 2 – Pyrolysis and ignition times plotted as a function of different heat fluxes [8].

### 1.3.1.2. The gas phase

The gas phase is a more complex phenomenon to be understood and described, and therefore it is normally less utilized. Once the solid is heated and pyrolysis process starts, the volatiles that are release mix with an oxidizer (e.g. air). When the mixture



reaches the lower or lean flammability limit (LFL), the mixture will ignite in the presence of an external heat source, such as a pilot flame or a spark. The process of ignition, therefore, requires that the volatiles that were already released feed enough heat back to the material, so more volatiles are emanated from the surface until a lean flammability limit can be achieved.

When modelling ignition, the use of a hot spot (e.g. pilot flame) simplifies the gas phase phenomena analysis. This is due to the fact that, in these cases, it can be assumed that ignition will happen as soon as the LFL is reached, and therefore no heat transfer between phases needs to be assessed. This leads to the assumption that  $t_{chem}$  and  $t_{mix}$  equal zero [3].

Here the concept of flash point and fire point that is related to liquid fuels is also applicable. The former concerns the first flash observed once ignition is achieved, i.e. the partial vapour pressure of the volatiles released reached the LFL. In this case, the flames are not self-sustaining, since there are not enough pyrolyzates to continue combustion reactions. This is due to the thermal inertia of the fuel, which leads to a slow response to the feedback from the flame, and therefore temperature does not increase enough to provide the required amount of volatiles. The latter is related to the moment when the rate of fuel supply is high enough to lead to chemical time shorter than residence time. In this case, the flame temperature is high enough to provide the necessary feedback to the solid that will lead to a fuel supply that is required for a self-sustaining flame. This concept is related to the Damköhler number, which is the ratio between residence time and chemical time, or reaction rates and diffusion rates. Figure 3 shows graphically this increase in the temperature which differs the flash point to the fire point in a solid fuel [3].

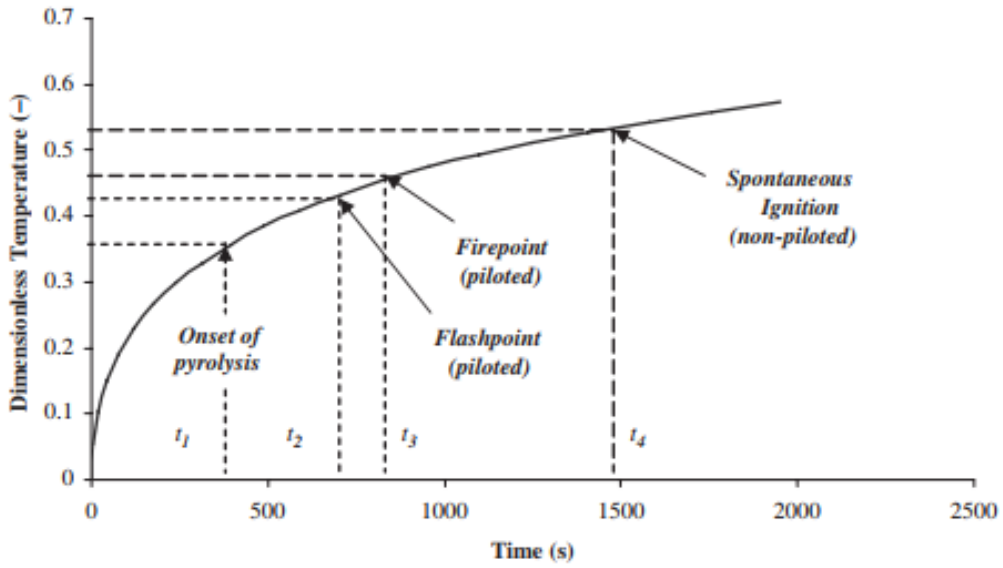


Figure 3 – Increase in the surface temperature of a solid with time and the different steps that are undergone by the solid fuel [9].

In an experimental procedure, the flow field can be assumed to be the same, and hence the residence time will remain constant for all experiments. Therefore, the chemical time will be the only varying parameter, which is related to the critical mass flux and can be quantified [2].

### 1.3.2. Heat transfer process

The heat transfer is the main process governing ignition. Ignition theory is based on solving the heat transfer at the solid surface and within the solid thickness [10].

The energy balance at the surface ( $x = 0$ ) under radiative heating at a time  $t$  is given by [11].

$$\dot{q}_{net}(0, t) = \alpha \dot{q}_i - \varepsilon \sigma (T^4(0, t) - T_\infty^4) - h_c (T(0, t) - T_\infty) \quad (1)$$

Where  $\dot{q}_{net}(0, t)$  is the net heat flux at the surface of the solid ( $x = 0$ ) at a time  $t$  [ $\text{kW}/\text{m}^2$ ],  $\alpha$  is the absorptivity,  $\dot{q}_i$  is the incident heat flux [ $\text{kW}/\text{m}^2$ ],  $\varepsilon$  is the emissivity,  $\sigma$  is the Stefan-Boltzmann constant [ $\text{W}/\text{m}^2\text{s}^4$ ],  $T(0, t)$  is the surface temperature ( $x = 0$ ) at a time  $t$  [K],  $T_\infty$  is the ambient temperature [K] and  $h_c$  is the convective heat transfer coefficient [ $\text{W}/\text{m}^2\text{K}$ ].

By assuming a linear approximation for the surface reradiation, the radiative term can be written as:

$$\varepsilon\sigma(T^4(0, t) - T_\infty^4) = h_r(T(0, t) - T_\infty) \quad (2)$$

Equation 2 can then be replaced in Eq. 1, and a total heat transfer coefficient can be used, which is a sum of the radiative and convective heat transfer coefficients. The energy balance at the surface of the solid sample then becomes:

$$\dot{q}_{net}(0, t) = \alpha\dot{q}_i - h_T(T(0, t) - T_\infty) \quad (3)$$

Figure 4 shows the heat transfer mechanisms that take place in a layer within the pyrolysis depth ( $x < \varepsilon_p$ ) and the parameters involved are summarized in Table 2.

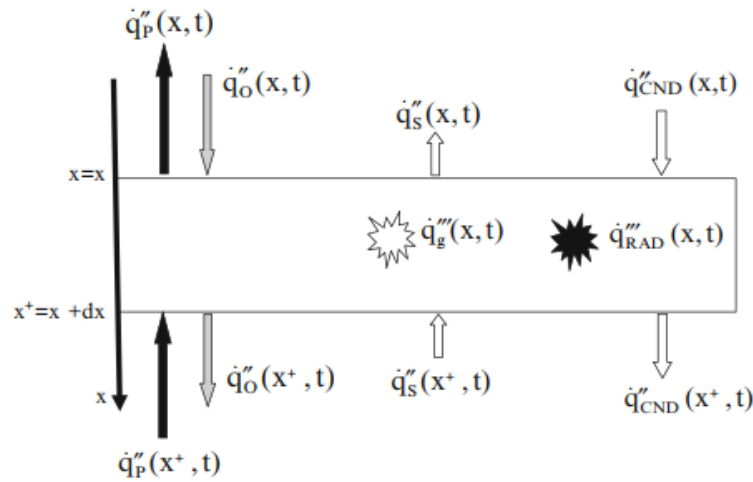


Figure 4 – Heat transfer mechanisms in a control volume for  $x < \varepsilon_p$  [3].

Table 2 – Summary of the parameters involved in the heat transfer for  $x < \varepsilon_p$  and their respective description [3].

Parameter	Description
$\dot{q}''_p(x, t)$ and $\dot{q}''_p(x^+, t)$	Energy transported by gaseous fuel travelling through the control volume
$\dot{q}''_o(x, t)$ and $\dot{q}''_o(x^+, t)$	Energy transported by oxygen travelling through the control volume
$\dot{q}''_s(x, t)$ and $\dot{q}''_s(x^+, t)$	Energy transported by solid fuel travelling through the control volume
$\dot{q}''_{CND}(x, t)$ and $\dot{q}''_{CND}(x^+, t)$	Heat transfer through conduction
$\dot{q}'''_{RAD}(x, t). dx$ and $\dot{q}'''_{RAD}(x^+, t). dx$	Radiative absorption
$\dot{q}'''_g(x, t). dx$	Chemical energy (generation/sink)

In lower heat flux levels, the heat waves penetrate deeper in the material, compared to higher levels [12]. It is essential to assess this thermal penetration, since the heat losses in the back surface of the material needs to be quantified in case the heat reaches this part of the solid, and the thickness of the material becomes a relevant dimension. This leads to the definition of thermal thickness. A thermally thin material is defined as the one where the thermal gradient can be negligible, whereas in a thermally thick material the thermal gradient is significant [3]. This can be assessed by a criterion called Biot number, presented in Eq. 4.

$$Bi = \frac{hL}{k} \quad (4)$$

Where  $h$  is the global heat transfer ( $W/m^2.K$ ),  $L$  is the solid thickness (m) and  $k$  is the solid thermal conductivity ( $W/m.K$ ). If  $Bi \ll 1$ , then the material is considered thermally thin, while if  $Bi \gg 1$  it is considered thermally thick.

### **1.3.3. Mass transfer process**

In most polymeric materials, the boiling temperature of the degradation products is lower than the polymer degradation temperature. This leads to a superheating process of these products, which nucleate and form bubbles [13].

Considering a thermally thick fuel, where the temperature gradient is high, the surface temperature is way higher than the temperature of the layers below, and therefore degradation is more significant there. The degradation process leads to a decrease in the molecular weight ( $M_w$ ), and the material viscosity is a function of this parameter and of temperature. Therefore, viscosity is lower near the surface than in the interior of the solid material in the presence of a thermal gradient, and this allows an easier migration of bubbles through the solid sample [6,11].

Kashiwagi observed that the incidence of bubble was much higher in the acrylic samples subjected to lower heat fluxes, as presented in Fig. 5.




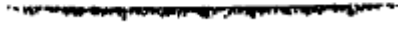

	$\dot{Q}_R''$ (kW/m <sup>2</sup> )	$t_{ig}$ (s)
	12	860
	15	450
	21	180
	27.5	102
	30	72

Figure 5 – Cross-sections of acrylic samples subject to different incident heat fluxes and their respective ignition delay time ( $t_{ig}$ ) [13].

According to Witkowski *et al.*, the physical swelling caused by the bubbling phenomenon leads to a reduction in the thermal inertia of the material, and hence to an acceleration in the rate of surface heating [3].

#### 1.3.4. The classic ignition theory

In order to predict when ignition might occur, or whether it occurs in a certain scenario or not, it is necessary to utilize an ignition criterion. The most utilized ones are based on solid-phase phenomena. Four different empirical criteria are presented on the literature, namely critical energy, critical temperature critical mass flux and time-energy squared [6].

The heat diffusion equation for a inert, one-dimensional and semi-infinite solid exposed to a radiative incident heat flux can be described as [5]:

$$\frac{\partial^2 \theta(x,t)}{\partial x^2} = \frac{1}{\alpha} \frac{\partial \theta(x,t)}{\partial t} \quad (5)$$

Where  $\theta(x,t) = T(x,t) - T_\infty$  and  $\alpha$  is the thermal diffusivity [m<sup>2</sup>/s]. The boundary conditions are expressed as [5]:

$$\begin{aligned} \dot{q}_{net}''(t) = \dot{q}_{ext}''(t) - h_r \theta(x,t) &= -k \frac{\partial \theta(x,t)}{\partial x}, x = 0 \\ \theta(x,t) &= 0, x \rightarrow \infty \end{aligned} \quad (6)$$

$$\theta(x, 0) = 0, \forall x$$

Where  $h_T$  is the total heat transfer coefficient, which comprises radiative and convective heat losses. It is assumed that radiative and convective heat losses take place at the exposed surface of the material.

The common analytical solution for Eq. 5 for constant incident heat fluxes is presented below [3, 5].

$$\frac{1}{\sqrt{t_{ig}}} = \frac{2}{\sqrt{\pi} \sqrt{k\rho c}} \cdot \frac{\dot{q}_{net}''}{\theta(0, t_{ig})} \quad (7)$$

Where  $\dot{q}_{net}''$  is the incident heat flux ( $\text{kW}/\text{m}^2$ ),  $k\rho c$  is the thermal inertia ( $\text{kW}^2\text{s}/\text{m}^4 \text{K}^2$ ),  $k$  is the conductivity ( $\text{kW}/\text{m.K}$ ),  $\rho$  is the density ( $\text{kg}/\text{m}^3$ ) and  $c$  is the specific heat ( $\text{kJ}/\text{kg.K}$ ). Also, here  $t_{ig}$  is assumed to be equal to the pyrolysis time ( $t_p$ )

Equation 8 is applicable under the assumption that ignition temperature is attained very fast, i.e.  $t_{ig} \ll t_c$ , where  $t_c$  is the characteristic temperature expressed by [3]:

$$t_c = \frac{\bar{k}_s \bar{\rho}_s \bar{c}_s}{(h_T)^2} \quad (8)$$

Although the conductivity, the density and the specific heat vary with temperature, here it is assumed to be constant, as a matter of simplification.

Figure 6 shows the ignition delay time, expressed as  $1/\sqrt{t_{ig}}$ , plotted as a function of the incident heat flux ( $\dot{q}_e''$ ). By using this graph and replacing the value of  $T_{ig}$  in Eq. 7 it is possible to extract the thermal inertia of the material. This is the product of thermal conductivity, density and specific heat ( $k\rho c$ ), and summarized the material properties that control flaming ignition of solid fuels. It is important to emphasize that the solid fuel is assumed to be semi-infinite.

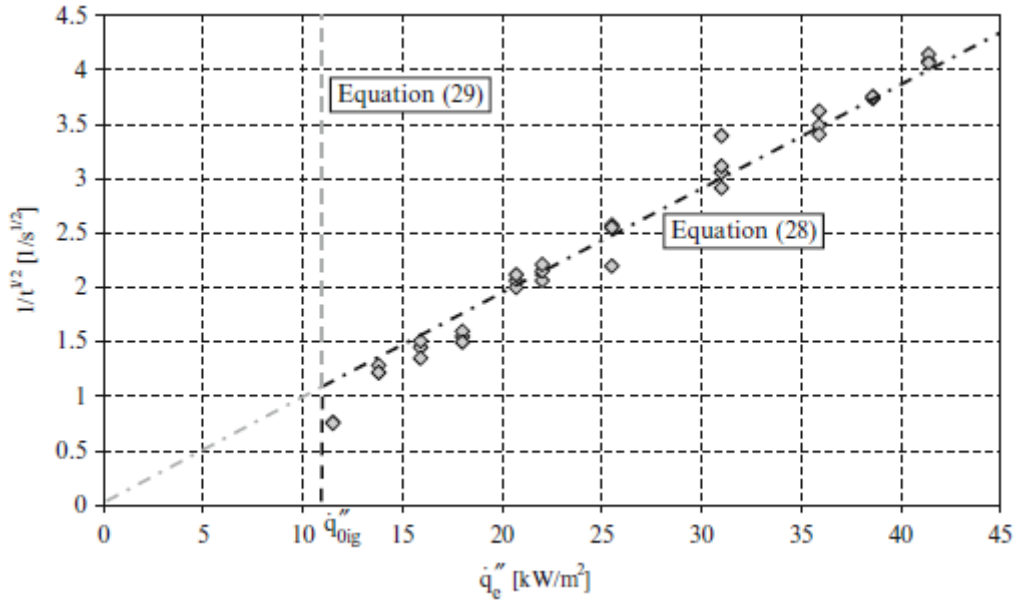


Figure 6 – Ignition delay time as a function of the incident heat flux for PMMA. Extracted from Chapter 21 of the SFPE Handbook of Fire Protection Engineering [3].

In the case of lower incident heat fluxes, where  $t_{ig} \gg t_c$ , Eq. 9 is used:

$$\frac{1}{\sqrt{t_{ig}}} = \frac{\sqrt{\pi} h_T}{\sqrt{k_s \rho_s c_s}} \left[ 1 - \frac{h_T (T_{ig} - T_\infty)}{\dot{q}''_e} \right] \quad (9)$$

Reszka *et al.* presented a solution for Eq. 5 considering a transient incident heat flux.

$$\frac{1}{\sqrt{t_{ig}}} = \frac{2}{\sqrt{\pi}} \frac{2}{3\sqrt{k\rho c}} \frac{\dot{q}''_{net}(t_{ig})}{\theta_{ig}} \quad (10)$$

Where  $\dot{q}''_{net}(t_{ig}) = \dot{q}''_{ext} - h_T \theta$ . Since it is assumed that the incident heat flux increases linearly,  $\dot{q}''_{ext} = mt - \dot{q}''_0$ . Also, in order to simplify the calculations and obtain Eq. 10, it is assumed that  $\dot{q}''_0 = 0$ .

The main limitation of this method regards the difficulty to measure the surface temperature. The main method currently used is measurement of temperatures throughout the thickness of the sample, so a suitable fit can be chosen and the surface temperature is found by extrapolation. This method is used in the present work. However, this method involves not only the uncertainties related to experiments, but also related to a mathematical approximation.

Moreover, it is assumed that the total incident heat flux is absorbed at the surface, i.e. the absorptivity equals 1. This leads to a failure in the method [14].

### **1.3.5. PMMA**

The main mechanism of decomposition is end-chain scission, which takes place when temperatures are relatively low (around 570 K). However, for higher temperatures (around 770 K), random-chain scission becomes the dominant initiation step. Moreover, this combination of random and end-chain scission is observed in the case of higher molecular weight PMMA. For the lower molecular weight ones, end-chain scission is the dominant mechanism. Also, when heated, PMMA decomposes into the monomer methyl methacrylate (MMA) and has a very large zip length, which is related to the number of monomers produced per single initiation event [3]. This break down process leads to a monomer yield of 91 to 98% by weight in thermal pyrolysis, but even under more extreme conditions (500°C) the monomer yield is around 80%. This simplifies the issues related to gas-phase chemistry and solid phase decomposition [7]. However, this is not the case in the present work, since the gas-phase is not assessed here.

PMMA is the most widely studied polymer due to the fact that its thermal decomposition process is relatively straightforward. Therefore, plenty of data is available on literature, which allows a better comparison of results with previous works [3].

### **1.3.6. Previous works**

In this section presents some results of previous works related to ignition. Data on critical MLR, ignition temperature and ignition delay time are presented in order to compare, later on, with the results obtained in the present work.

Reszka *et al.* [5] tested PMMA samples under transient incident heat fluxes in the Fire Propagation Apparatus (FPA). The samples measured 110 x 110 x 6 mm or 100 x 100 x 4.9 mm. The sample holder was an aluminium block, in order to assume a semi-infinite solid. The results for ignition delay time are presented in Table 3.



Table 3 – Ignition delay time for different heating rates. Extracted from [5].

HR [W/m <sup>2</sup> .s]	t <sub>ig</sub> [s]
30	609
50	428
100	273

Santamaria *et al.* [10] assessed PA6 samples under transient incident heat fluxes in the Fire Propagation Apparatus (FPA), and both solid and gas phases were studied. The samples measured 85 x 85 x 20 mm and were exposed to 7 different heating rates (40, 50, 60, 70, 80, 90 and 100 W/m<sup>2</sup>.s). Since the material studied is different than the one used in the present work, the results will be discussed only qualitatively. They observed a decrease in the time to ignition and an increase in the IHF at ignition with the increase in the heating rate, as illustrated in Fig. 7. The mass loss rate increased until the heating rate of 70 W/m<sup>2</sup>.s, but after that it starts to decrease (Fig. 8).

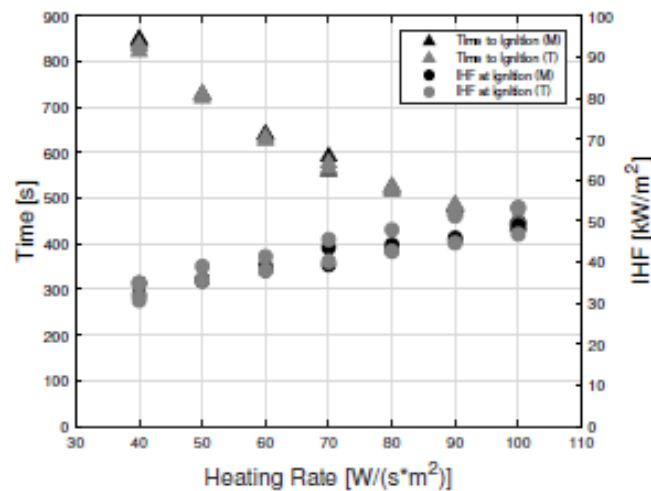


Figure 7 – Time to ignition and IHF at ignition as a function of the heating rate [10].

The net heat flux (NHF) and the critical surface temperature did not vary significantly with the heating rate. A mean value of  $4.4 \pm 1.4$  kW/m<sup>2</sup> was found for the NHF.

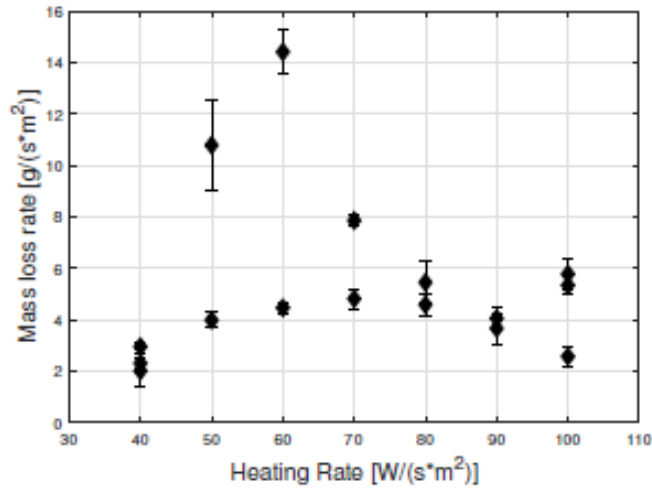


Figure 8 – Mass loss rate per unit area as a function of the heating rate [10].

Vermesi *et al.* [6] studied PMMA samples measuring 100 mm x 100 mm x 30 mm deep. The aim was to establish the parameter which is the most suitable to describe ignition under transient heating. The heating rates were parabolic-shaped, and a total of 16 pulses were utilized with peaks ranging from 25 to 45 kW/m<sup>2</sup> and time peaks from 280 to 480 s. The experiments were carried out using the Fire Propagation Apparatus (FPA). However, only temperatures were measured; the mass loss rate was predicted numerically using Gpyro. Also, experiments with constant incident heat flux were also performed, but using a cone calorimeter, and incident heat fluxes of 15 kW/m<sup>2</sup> and 20 kW/m<sup>2</sup> were applied. It was found that the critical mass loss rate, followed by critical temperature, were the ones providing best prediction, whereas the critical energy provided the worst prediction. The lowest values that led to ignition were 3 g/m<sup>2</sup> for MLR and 305°C for critical temperature. No ignition was obtained with 15 kW/m<sup>2</sup>, whereas for 20 kW/m<sup>2</sup> the ignition delay time was 520 s. Table 4 summarizes the results for ignition delay time, critical surface temperature and critical mass flux.

Table 4 – Summary of ignition conditions reported by Vermesi *et al.* for different scenarios. Data extracted from [6].

Experiment	$t_{ig}$ [s]	$T_{ig}$ [°C]	$\dot{m}''_{ig}$ [g/m <sup>2</sup> .s]
20 kW/m <sup>2</sup>	520	320	4.9
30 kW/m <sup>2</sup> at 320 s	450	360	5.2
45 kW/m <sup>2</sup> at 320 s	300	383	9.0
30 kW/m <sup>2</sup> at 480 s	475	335	4.1

Fereres *et al.* [15] assessed the mass flux at different pressure environments using the Forced-flow Ignition and Flame Spread Test (FIST). The samples measured 30 x 30 x 10 mm. They found that, for ambient pressure (100 kPa), the mass flux at ignition was approximately 2.1 g/m<sup>2</sup>s for a constant incident heat flux of 16 kW/m<sup>2</sup>.

Tewarson *et al.* [1] tested PMMA samples in the FMRC 50 kW-Scale Flammability Apparatus. The samples measures 10 mm x 10 mm x 25 mm thick. The ignition source was premixed ethylene-air pilot flame, located at 10 mm from the solid surface. The ignition temperature of black PMMA was reported to be 655 K, assuming that convective heat losses are negligibly small. This value is very close to the value of 651 K for 12 mm thick PMMA, reported in the SFPE Handbook of Fire Protection Engineering [3].

Lyon *et al.* [16] looked at both solid and gas phase. For the former, the parameters analysed were ignition temperature and critical heat flux, whereas for the latter, the mass flux and heat release rate at flash point and fire point. The results are shown in Tables 5 and 6.

Table 5 – Results obtained by Lyon *et al.* for different parameters at ignition by looking at the solid phase [16].

<b>Parameter</b>		<b>Calculated</b>	<b>Measured</b>
Solid phase	Ignition Temperature (°C)	304	280 - 320
	Critical heat flux (kW/m <sup>2</sup> )	11	6.0 - 23.0

Table 6 – Results obtained by Lyon *et al.* for different parameters at ignition by looking at the gas phase [16].

<b>Parameter</b>		<b>Flash point</b>	<b>Fire point</b>
Gas phase	Mass flux (g/m <sup>2</sup> .s)	0.97 - 1.01	1.9 - 3.2
	HRR (kW/m <sup>2</sup> )	25	61

Rhodes [17] studied samples of black polycast PMMA measuring 100 mm x 100 mm x 25 mm thick in a cone calorimeter. The thermocouples were placed at the surface of the sample by soldering iron. Heat fluxes from 0 to 75 kW/m<sup>2</sup> were applied. It was observed that, for lower incident heat fluxes, the ignition temperature varied significantly, whereas for higher heat fluxes it is roughly constant. For the former case, temperatures

in the range of 250°C were observed (for IHF of 15 kW/m<sup>2</sup>), and in the latter, temperatures in the range of 350°C (for IHF greater than 45 kW/m<sup>2</sup>) [17]. In order to better visualize the trend in the ignition delay time with the incident heat flux, a graph was plotted with the results obtained and is illustrated in Fig. 9. The values obtained for ignition delay time ( $t_{ig}$ ) and critical surface temperature ( $T_{ig}$ ) are presented in Table 7. Although a wide range of results were obtained in this work, only the ones related to the incident heat flux of 19 and 50 kW/m<sup>2</sup> are presented in the table due to the fact that in this thesis constant incident heat fluxes of 20 and 50 kW/m<sup>2</sup> were utilized.

Table 7 – Ignition delay times and ignition temperature for black PMMA for the heat fluxes 19 and 50 kW/m<sup>2</sup> obtained by Rhodes [17].

IHF (kW/m <sup>2</sup> )	$t_{ig}$ (s)	$T_{ig}$ (°C)
19	141	265
	135	
50	20	-
	25	
	26	
	22	

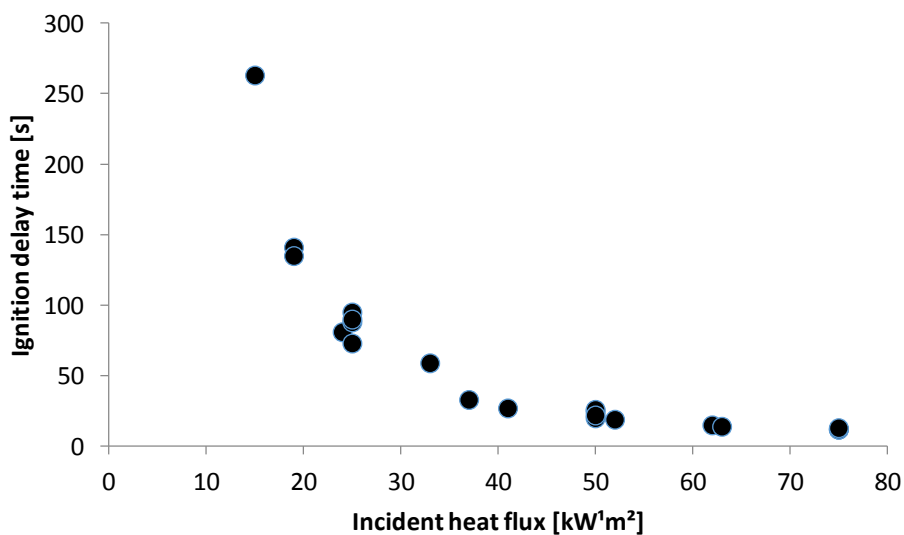


Figure 9 – Ignition delay time as a function of the incident heat flux for black PMMA. Data extracted from Rhodes [18].

Rich *et al.* [19] studied PMMA samples under different environmental conditions, such as heat flux, oxygen concentration and oxidizer flow velocity. The experiments were carried out in the Forced Ignition and Flame Spread Test apparatus (FIST), and IHFs of 10 to 45 kW/m<sup>2</sup> were utilized. It was observed an increase in the critical mass flux with the increase in the incident heat flux. The critical MLR was assessed at both flash and fire points. Figure 10 shows the results obtained for the experiments with normal air and freestream velocity of 1.0 m/s .

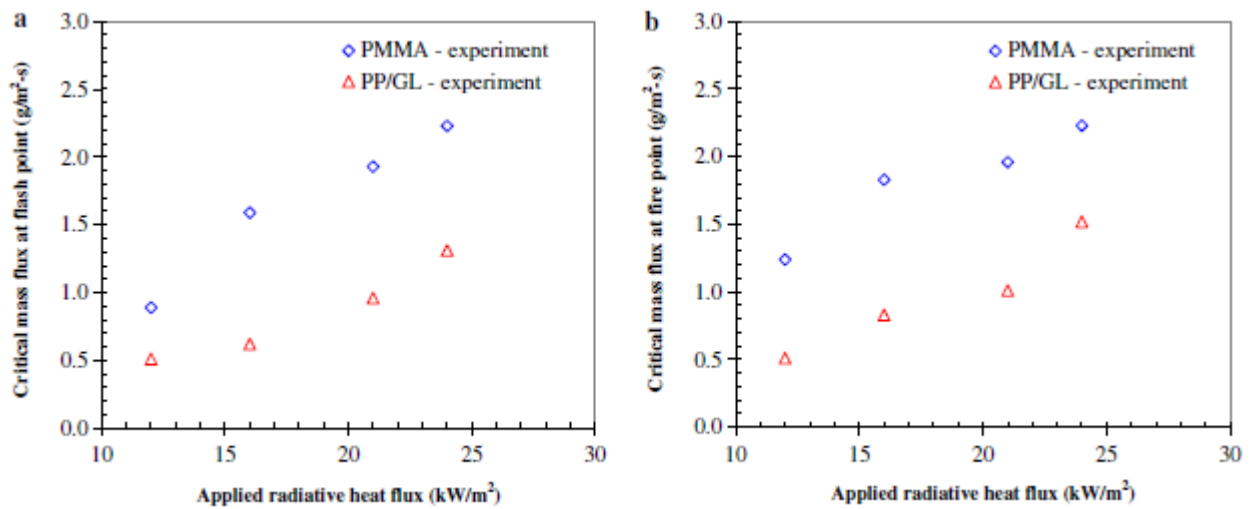


Figure 10 – Critical mass flux for different incident heat fluxes at (a) flash point and (b) fire point [19].

Link [7] studied cylindrical PMMA samples, both black and clear ones placed vertically. The apparatus was a combustion chamber enclosed by a quartz tube, with halogen lamps providing constant heat fluxes. The ignition source was a wire coil placed at 15 mm downstream and 15 mm from the lateral sample surface (around the radius). All critical mass flux results were found to be below 1.0 g/m<sup>2</sup>·s. The results were compared with previous literature, as showed in Fig. 11, of which two [12,13] were previously discussed in the present work.

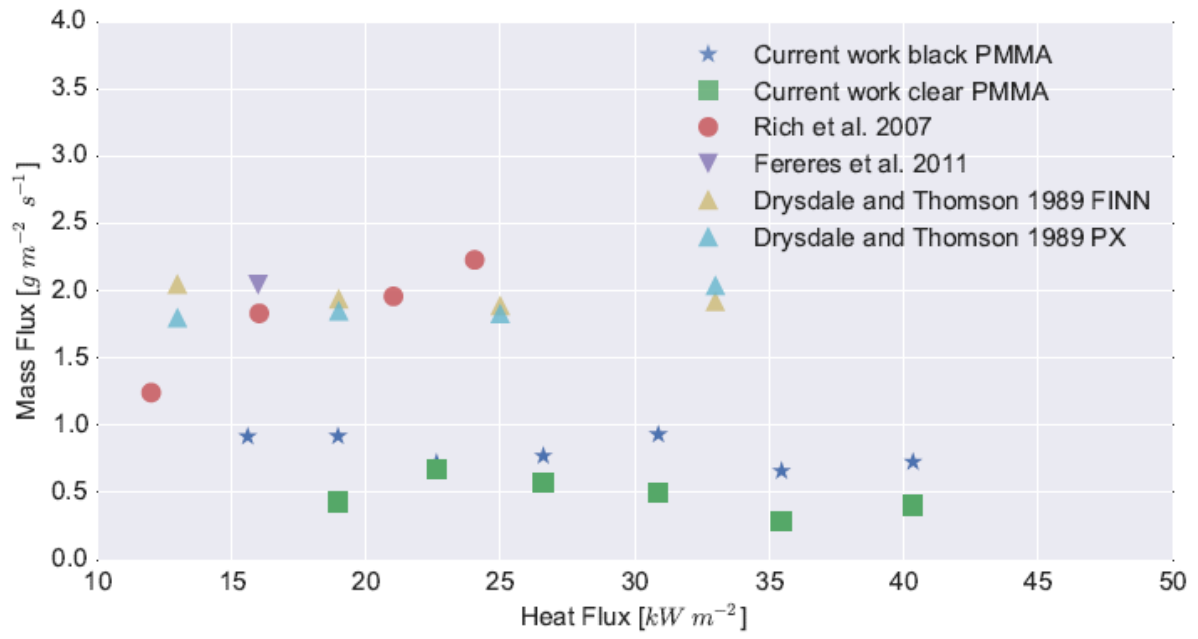


Figure 11 – Comparison between results from previous works for critical mass flux. Extracted from [7].



## CHAPTER 2

### METHODOLOGY

#### 2.1. Samples preparation

The material assessed in the present work was black polymethyl methacrylate (PMMA), with density of  $1190 \text{ kg/m}^3$ , thermal conductivity of  $0.19 \text{ W/m.K}$  and specific heat of  $1.4 \text{ kJ/kg.K}$ . The material properties were extracted from Link [7].

The sample size was  $85 \times 85 \times 25 \text{ mm}$ . They all had the sides covered with two layers of insulation paper, with thickness of  $1 \text{ mm}$  each. The aim is to assume that heat losses will take place at the back and the front surfaces of the sample. The insulation paper has a density of  $150 \text{ kg/m}^3$  and melting point of  $2000^\circ\text{C}$ .

An aluminium block measuring  $90 \times 90 \times 20 \text{ mm}$  was used as a sample holder. By doing so, it can be assumed that all the heat losses will occur in the front surface (radiative and convective) and in the back surface (conductive, to the aluminium block) and the solid fuel can be treated as semi-infinite.

In order to enhance the conductive heat transfer from the solid sample to the aluminium block, a heat sink paste was applied in the back surface of the sample. Figure 12 shows the samples used for the mass loss experiments.



Figure 12 – Front (left-hand side) and back (right-hand side) surfaces of the samples for mass experiments.



For the temperature experiments, the samples were drilled in the Laboratory 2 at the University of Edinburgh. The thermocouples were placed at heights of 4, 8, 12 and 16 mm from the surface. Figure 13 shows a sample used for the temperature experiments. A schematic of the position is shown in Fig. 14.



Figure 13 – Sample used for temperature experiments.



Figure 14 – Schematic of the thermocouple position in the sample.

The experiments were identified as presented below:

$$\underline{X-YY-Z-A}$$

Where

X = Transient (T) or constant (C) heat flux.

YY = Value of heating rate (HR) or incident heat flux (IHF)

Z = Sample number

A = Mass (M) or Temperature (T) experiment

The samples identification is presented in Tables 8, 9, 10 and 11.

The ones marked with an asterisk (\*) were only used for ignition delay time and incident heat flux at ignition. This is due to the fact that the results obtained were not good, and therefore they were discarded in the analysis of MLR or Temperature (surface temperature and heat losses calculations).

Table 8 – Sample identification for the mass loss experiments under transient conditions.

<b>HR [W/m<sup>2</sup>.s]</b>	<b>Sample name</b>
40	T-40-1-M
	T-40-2-M
	T-40-3-M
	T-40-4-M *
60	T-60-1-M *
	T-60-2-M
	T-60-3-M
	T-60-4-M
	T-60-5-M
	T-60-6-M
'80	T-80-1-M
	T-80-2-M
	T-80-3-M *
	T-80-4-M
	T-80-5-M *

Table 9 - Sample identification for the mass loss experiments under constant incident heat flux.

<b>IHF (W/m<sup>2</sup>.s)</b>	<b>Sample name</b>
20	C-20-1-M
	C-20-2-M
50	C-50-1-M
	C-50-2-M

Table 10 - Sample identification for the temperature experiments under transient conditions.

HR (W/m <sup>2</sup> .s)	Sample name
40	T-40-1-T *
	T-40-2-T
	T-40-3-T
60	T-60-1-T
	T-60-2-T
	T-60-3-T
80	T-80-1-T
	T-80-2-T
	T-80-3-T
	T-80-4-T*
	T-80-5-T*

Table 11 - Sample identification for the temperature experiments under constant incident heat flux.

IHF (kW/m <sup>2</sup> )	Sample name
20	C-20-1-T
	C-20-2-T
50	C-50-1-T
	C-50-2-T

## 2.2. The Fire Propagation Apparatus (FPA)

The Fire Propagation Apparatus (FPA) consists in a heat release calorimeter used to quantify different material flammability characteristics, which includes time to ignition ( $t_{ig}$ ), chemical heat release rate ( $\dot{Q}_{chem}$ ), convective heat release rate ( $\dot{Q}_c$ ), mass loss rate ( $\dot{m}$ ) and effective heat of combustion (EHC) [1]. The main difference between the FPA and the Cone Calorimeter is the fact that in the former it is possible to place an infrared transparent quartz tube and, therefore, form a combustion chamber, which prevent the pyrolysis gases to be blown away [20]. Moreover, the use of a transient heat flux is only possible on the FPA.

The three tests that are performed by using the FPA are:

- a) Ignition Test, which is used to determine the time to ignition;
- b) Combustion Test, which is used to determine  $\dot{Q}_{chem}$ ,  $\dot{Q}_c$ ,  $\dot{m}$  and EHC;
- c) Fire Propagation Test, is used to determine  $\dot{Q}_{chem}$  of vertical specimens and the Fire Propagation Index (FPI).

The Ignition and Combustion tests apply for horizontal specimens, whereas the Fire Propagation applies for vertical ones.

In the present work, the Ignition Test was carried out with scale and thermocouples attached to the apparatus. Figure 15 shows a schematic view of the FPA.

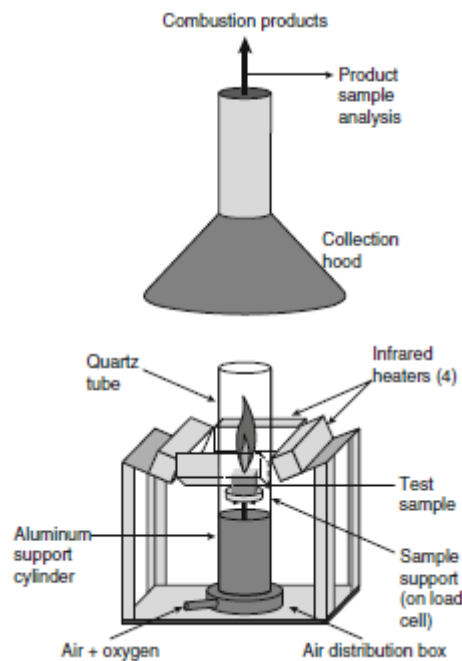


Figure 15 – Schematic of the Fire Propagation Apparatus (FPA). Extracted from Chapter 36 of the SFPE Handbook [3].

### 2.3. Description of the experiments

Three different heating rates were used, 40, 60 and 80 W/(m<sup>2</sup>.s). The experiments for MLR and temperature were performed separately, in order to avoid any impact of the thermocouples in the mass measurements.

A quartz tube was used in order to obtain a combustion chamber. The inlet flow of air was set to 200 lpm. The ignition source was a premixed ethylene-air pilot flame located

at 10 mm from the sample surface and 10 mm from the lateral edge of the sample. Also, the length of the pilot flame was adjusted to 10 mm [21].

As aforementioned, most of the previous works were based on constant incident heat flux. Therefore, experiments using constant heat flux were also carried out, in order to obtain a comparison with literature. Two different values for IHF were used, 20 and 50 kW/m<sup>2</sup>. Figures 16 and 17 show the experimental set-up for mass loss and temperature experiments, respectively, in the Fire Propagation Apparatus.

For all experiments, the ignition delay time was recorded and compared for different heating rates and constant IHF. For transient heating, the incident heat flux at ignition was also compared.

It is important to point out that, for the experiments using constant heat flux, a new heat flux gauge was used. Also, for all experiments using a transient heating the same previous heat flux gauge was utilized.

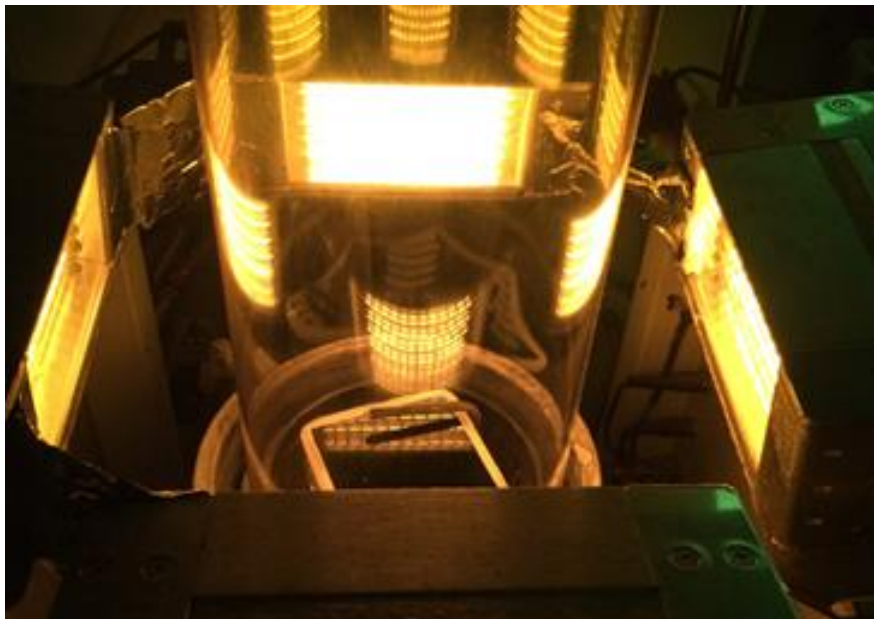


Figure 16 – Experimental set-up for mass loss experiments in the Fire Propagation Apparatus.

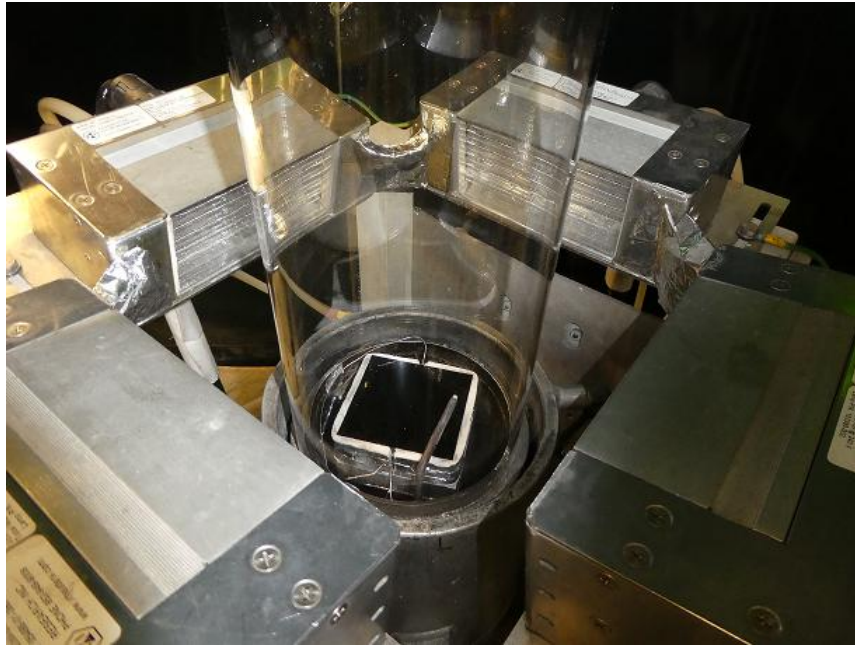


Figure 17 – Experimental set-up for temperature experiments in the Fire Propagation Apparatus.

#### 2.4. Mass Loss Rate (MLR) measurements

For the mass loss recording, a Metler Toledo load cell model WMS4002-L was used, with a mass measurement error of 0.01 g. Once the results were obtained, the mass per unit area was plotted against time. A different trend in the curve is observed close to ignition, and this interval was used for the MLR calculation. This varied for the different experiments, but the overall range varied between 4 and 10 s. A linear fit was then applied and the correspondent equation was used to determine the gradient of the curve, which corresponds to the mass loss rate. This methodology is represented in Fig. 18, where the first graph (a) is the curve Mass vs. Time for the entire duration of the experiment and the second (b) is the last data points of the graph, which represents the visual analysis of the mass loss rate. It is important to emphasize that, in the second graph, the mass was divided by the surface area (0,085 x 0,085 m) in order to obtain the mass loss rate per unit area [ $\text{g}/\text{m}^2.\text{s}$ ].

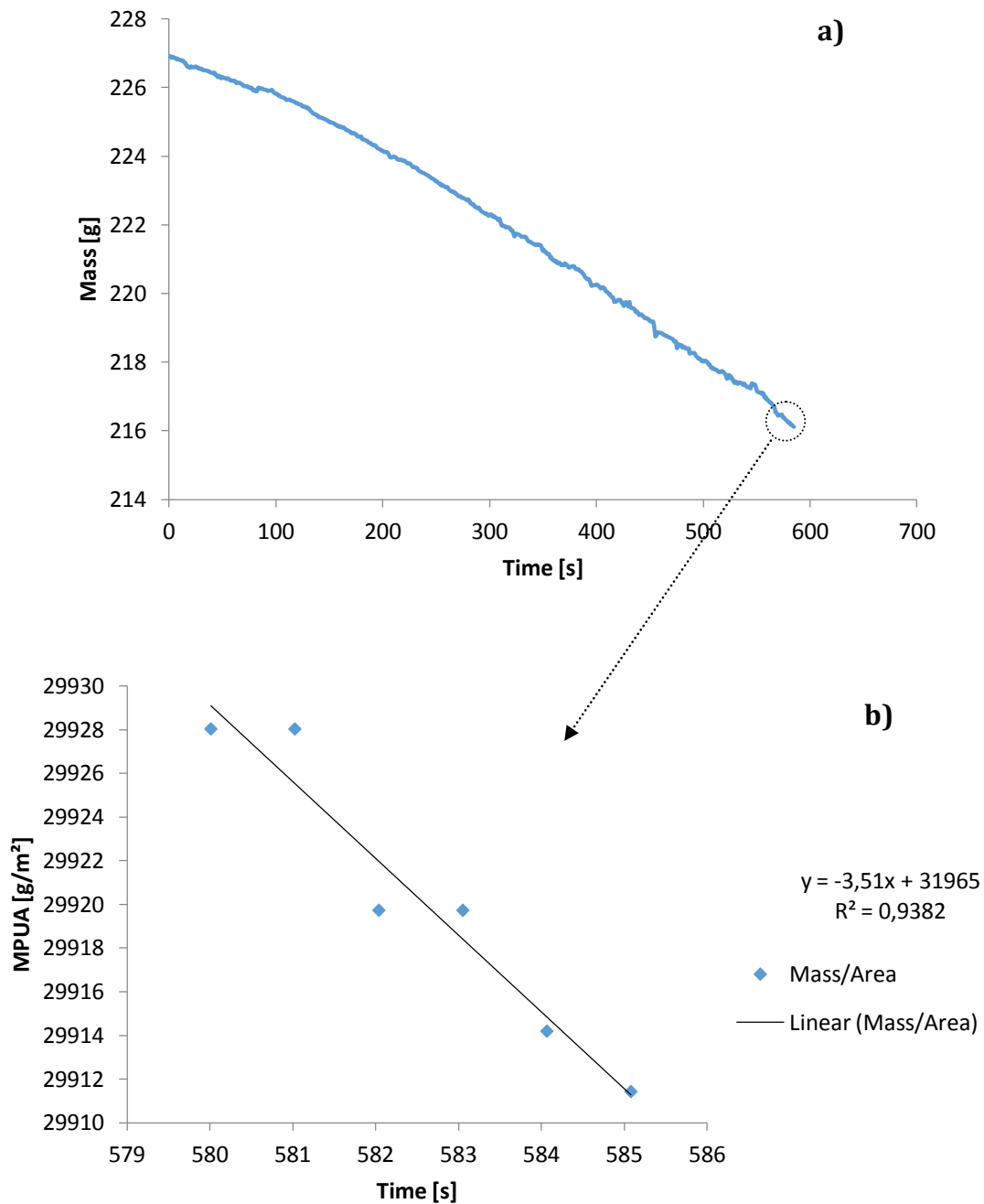


Figure 18 – Graphs plotted from sample T-40-2-M illustrating the methodology used for the MLR calculation; a) Mass as function of time for the whole experiment and b) Zoom from a) showing the mass per unit area plotted against time and the linear fit according to visual analysis.

The linear fit was applied also to a fixed time interval of the last 10 seconds for all the experiments. This procedure aims to compare different experiments at the same interval choice, i.e. establishing a standard time interval for all cases. Moreover, this method also aims to evaluate how the interval choice affects the results. The results were compared to the ones obtained with the visual analysis of the mass loss rate. This

provides an understanding of how the interval choice affects the results and somehow illustrates how the mass loss rate changes close to ignition.

In the graphs containing the average mass loss rate as function of the heating rate, error bars were plotted based on the difference between the average value and the maximum (Error +) and minimum (Error - ) values.

## 2.5. Temperature

For the temperature experiments, four type K thermocouples with 2 mm diameter were placed in the PMMA sample and one in the aluminium. The temperature measurements in the solid sample were used to estimate the surface temperature at ignition and also to calculate the heat losses, whereas the one in the aluminium block was used to quantify the conductive heat losses. One-dimensional heat transfer is assumed. Figures 19 and 20 show details on the experimental set-up and the position of the thermocouples.

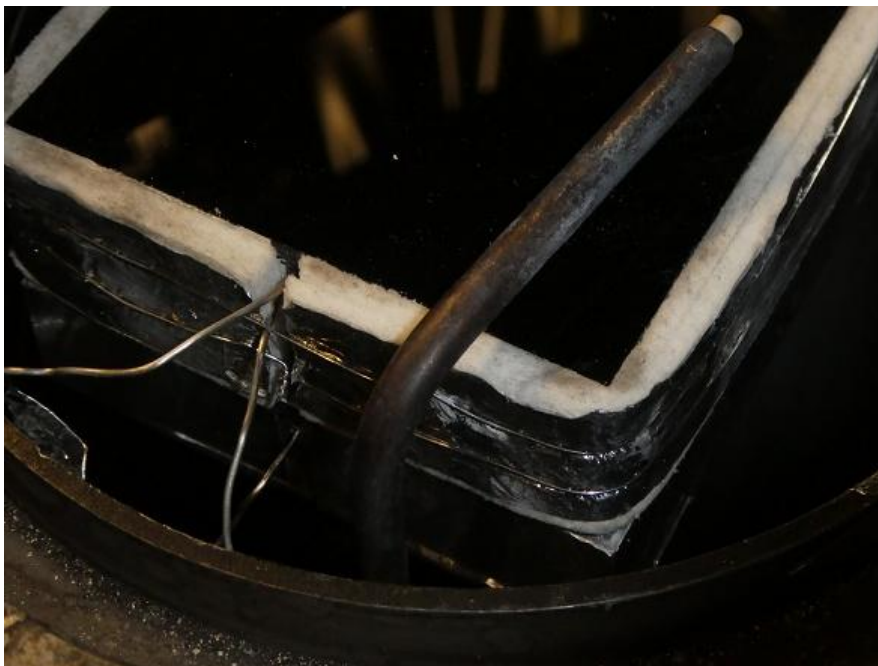


Figure 19 – Detail on the thermocouples position at 4, 12 mm and in the aluminium block.





Figure 20 – Top view from the experimental set-up for temperature experiments.

In the all graphs containing an average as function of the heating rate, such as surface temperature and heat losses, error bars were plotted based on the difference between the average value and the maximum (Error +) and minimum (Error - ) values.

### 2.5.1. *Surface temperature*

For the surface temperature measurement, the temperatures from each point at ignition were plotted against depth. A quadratic fit was used in order to describe the temperature distribution in the solid. Once the equation is obtained, it is possible to do an extrapolation and determine the surface temperature, by taking the surface of the sample as  $x = 0$ .

### 2.5.2. *Heat losses*

The heat losses calculations are divided into two, the radiative and convective heat losses at the top surface of the solid sample and the conductive heat losses through the back of the sample.

By taking the surface of the sample as a control volume, the energy balance can be calculated with Eq. 11.

$$\dot{q}_{inc} = \dot{q}_{loss} + \dot{q}_{net} \quad (11)$$

Where  $\dot{q}_{inc}$  is the irradiation that reaches the solid surface,  $\dot{q}_{loss}$  are the surface losses, which include radiation and convection, and  $\dot{q}_{net}$  is the net heat flux that is absorbed by the sample at the surface.

However, if the control volume is the whole sample,  $\dot{q}_{net}$  can be replaced as shown in Eq. 12, and Eq. 11 can be rewritten as Eq. 13.

$$\dot{q}_{net} = \dot{q}_{cond} + \dot{q}_{pyr} + \dot{q}_{end} + \dot{q}_{sto} \quad (12)$$

$$\dot{q}_{inc} = \dot{q}_{loss} + \dot{q}_{cond} + \dot{q}_{pyr} + \dot{q}_{end} + \dot{q}_{sto} \quad (13)$$

Where  $\dot{q}_{cond}$  represents the conductive losses at the back of the sample to the aluminium block,  $\dot{q}_{pyr}$  is the heat of pyrolysis,  $\dot{q}_{end}$  stands for the endothermic reactions and  $\dot{q}_{sto}$  is the energy flux stored in the sample.

For the surface losses calculations ( $\dot{q}_{loss}$ ), Equation 8 was used, where  $\dot{q}_{inc}$  is the incident heat flux at each data point and  $\dot{q}_{net}$  was obtained by using Fourier's law (Eq. 14).

$$\dot{q}_{net} = -k \cdot \frac{dT}{dx} \quad (14)$$

For the conductive heat losses ( $\dot{q}_{cond}$ ) calculations, the temperature of the aluminium block was utilized and  $k = 0.2 \text{ W/m.k}$ . A thermocouple was placed at 5 mm from the surface in contact with the sample. The conductive losses were calculated with Eq. 15.

$$\dot{q}_{cond} = \frac{m \cdot c \cdot \Delta T}{A} \quad (15)$$

Where  $m = 392 \pm 0.01 \text{ g}$ ,  $c = 0.91 \pm 0.01 \text{ kJ/kg.K}$ ,  $A = 0.0072 \pm 0.0002 \text{ m}^2$  and  $\Delta T$  is the aluminium block temperature, and was calculated at each data point in the Excel spreadsheet. The value at ignition was taken as the  $\dot{q}_{cond}$ . The values used for the mass and specific heat were extracted from [10].

## 2.6. Propagation of uncertainties

In order to take into consideration the uncertainties related to the measurements of mass, specific heat and surface area of the aluminium block, the propagation of uncertainties method was used. The uncertainty in the conductive heat losses ( $\delta \dot{q}_{cond}$ ) is calculated with Eq. 16.

$$\delta \dot{q}_{cond} = \sqrt{\left(\frac{\partial \dot{q}_{cond}}{\partial m} \cdot \delta m\right)^2 + \left(\frac{\partial \dot{q}_{cond}}{\partial c} \cdot \delta c\right)^2 + \left(\frac{\partial \dot{q}_{cond}}{\partial A} \cdot \delta A\right)^2} \quad (16)$$

Where:

$$\frac{\partial \dot{q}_{cond}}{\partial m} = \frac{c}{A} \cdot \left(\frac{\partial T}{\partial t}\right) \quad (17)$$

$$\frac{\partial \dot{q}_{cond}}{\partial c} = \frac{m}{A} \cdot \left(\frac{\partial T}{\partial t}\right) \quad (18)$$

$$\frac{\partial \dot{q}_{cond}}{\partial A} = \ln(A) \cdot m \cdot c \cdot \left(\frac{\partial T}{\partial t}\right) \quad (19)$$

And  $\delta m = 0.00001$  kg,  $\delta c = 0.01$  kJ/kg.K and  $\delta A = 0.0002$  m<sup>2</sup>.

The derivative  $\partial T/\partial t$  was calculated by plotting the curve Temperature vs. Time for the thermocouple and a quadratic fit was used and the derivative of the equation was used (Fig. 21). The time used was the ignition delay time.

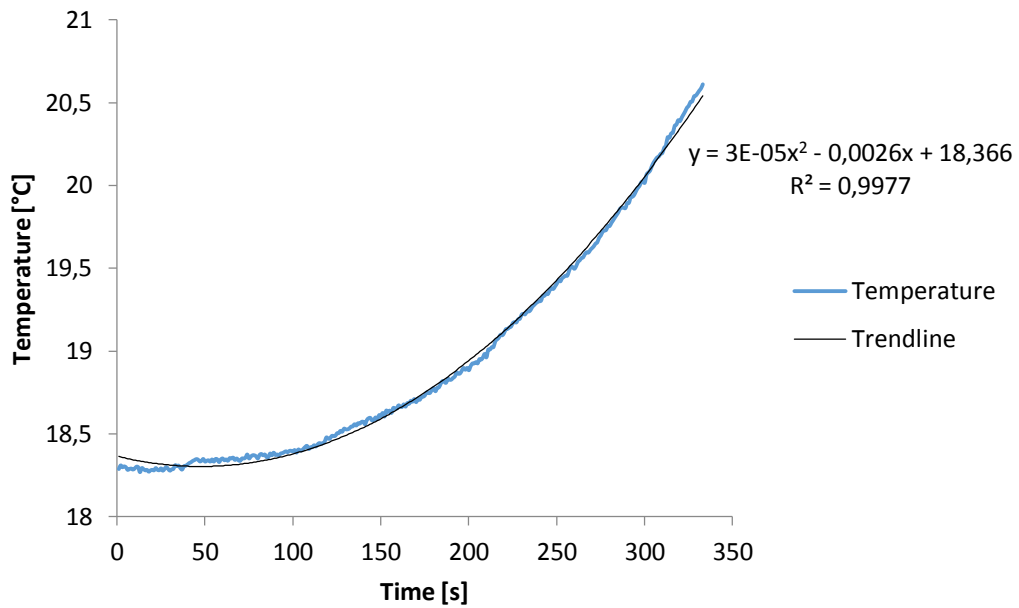


Figure 21 – Temperature vs. Time for the aluminium block temperature. Sample T-80-2-T (subjected to a heating rate of 80 W/m<sup>2</sup>.s)

## CHAPTER 3

### RESULTS AND DISCUSSION

#### 3.1. MLR experiments

In this section, the results are discussed separately for transient and constant heating.

##### 3.1.1. Transient heating

As explained in 2.4, different time intervals were chosen based on visual analysis and last 10 seconds. Figure 22 shows the results for MLRPUA for the visual analysis, whereas Fig. 23 shows the ones based on the last 10 seconds for all samples. The results are also summarized in Table 12, which shows both average values for mass loss rate and standard deviation.

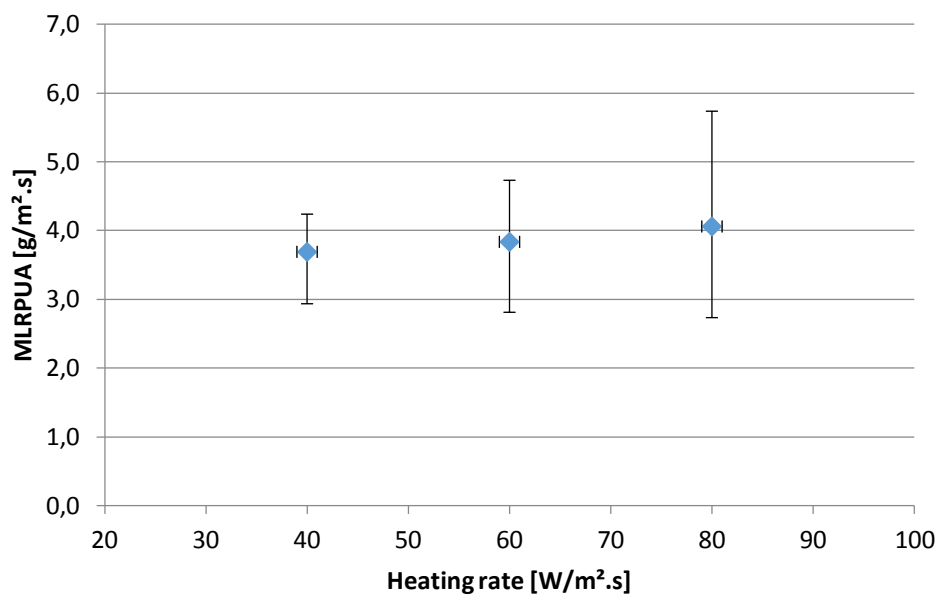


Figure 22 – Mass loss rate per unit area calculated based on a visual analysis.

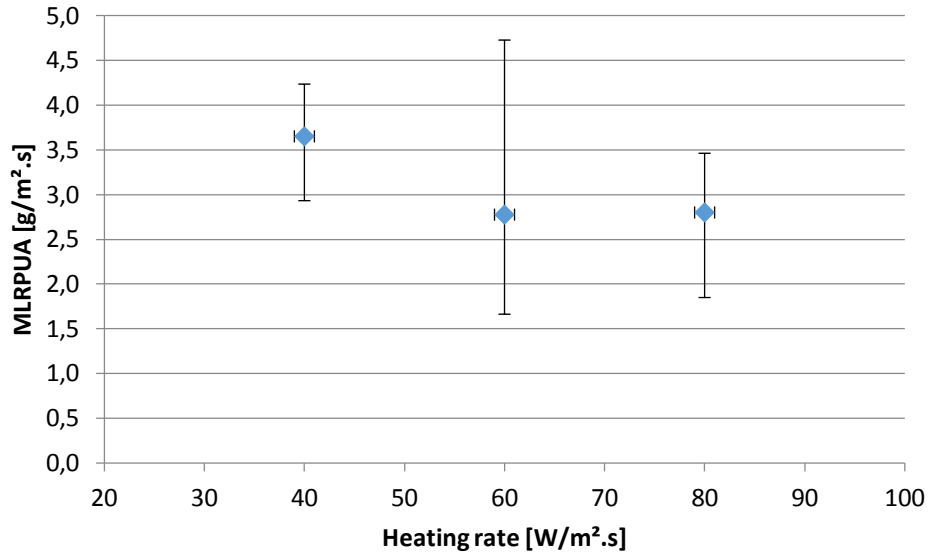


Figure 23 – Mass loss rate per unit area calculated based on the last 10s.

Table 12 – Summary of results for MLR based on the visual analysis and last 10 seconds intervals.

Heating rate [W/m <sup>2</sup> ]	Visual analysis			Last 10 s		
	Average [g/m <sup>2</sup> .s]	Error +	Error -	Average [g/m <sup>2</sup> .s]	Error +	Error -
40	3,6859	0,5496	0,7541	3,6507	0,5848	0,7189
60	3,8313	0,8964	1,0234	2,7754	1,9523	1,1126
80	4,0559	1,6769	1,326	2,8002	0,6618	0,9513

The results are both quantitatively and qualitatively different. In the results based on the visual analysis, an increase in the MLRPUA is observed with the increase in the heating rate, whereas the results based on the last 10 seconds show a decrease with the heating rate. This means that the results are very sensitive to the interval choice, and therefore reflects this trend of a change in the mass loss rate close to ignition.

The errors were significantly high for both cases (visual observation and 10 s), and that affects the reliability of the trend.

The values obtained for MLR based on the visual analysis are used to compare with results from previous works, since it is a more reasonable approach in a methodological viewpoint due to the fact that it encompasses the trend described above for the MLR at

ignition. Moreover, the results obtained with the visual analysis are qualitatively in accordance with the observations of Links [7], where an increase in the MLR with the IHF was also reported. Although they used a constant incident heat flux, these results can be compared due to the fact that a higher heating rate implies that, for the same time interval, more heat is provided (higher incident heat flux at the same test time). Moreover, the incident heat flux at ignition was greater at higher heating rates, which will be discussed in 3.3.

A comparison between the results obtained in this thesis and the literature is summarized in Table 13.

Table 13 – Comparison between the values from literature and the ones obtained in the present work.

<b>Author</b>	<b>Condition</b>	<b>MLRPUA [g/m<sup>2</sup>.s]</b>
Fereres et al.	16 kW/m <sup>2</sup>	2.1
Lyon	-	1.9 - 3.2
Rich et al.	22 kW/m <sup>2</sup>	2.3
Drysdale	25 kW/m <sup>2</sup>	1.7
Vermesi	20 kW/m <sup>2</sup>	4.9
Vermesi	Peak of 30 kW/m <sup>2</sup>	5.2
Present work	40 W/m <sup>2</sup> .s	3.6859
Present work	60 W/m <sup>2</sup> .s	3.8313
Present work	80 W/m <sup>2</sup> .s	4.0559

Rich *et al.* [19] stated that, at higher incident heat fluxes, the oxidizer permeates more easily at the heated surface layer of the material that is undergoing pyrolysis. Oxidative reactions will take place in this thin layer and thus will prevent that some of the pyrolyzate gases reach the flame front. Consequently, higher mass flux is required in order to reach the LFL.

Another explanation, also presented by Rich *et al.*, is related to the bubbling phenomenon, which will be further discussed in 3.4. In the experiments carried out for the present work, bubbles were smaller and released more quickly. This means that more pyrolyzates reach the surface, and therefore diffusion and mixing with the oxidizer is more difficult, so a higher mass flux is required to reach the LFL .

Although the boundary condition is different in the present work, i.e. a transient irradiation is utilized, the comparison is done based on the fact that higher HR imply higher IHF and, therefore, more energy absorbed by the material for a certain time interval. Moreover, the IHF was found to be higher at higher HR. However, it is important to emphasize that, in most cases, the constant heat flux imply higher heating rates, which in turn should lead to higher values of critical mass flux.

Several uncertainties explain the errors. Firstly, the uncertainty in the measurement taken by the scale, which is extremely sensitive to external perturbations. Secondly, the linear fit and the interval choice. There is an error associated to the linear fit, which is expressed by the linear regression ( $R^2$ ), which means that there are deviations between the calculated and the real values. The visual observation is very subjective and affect directly the result, as shown in the comparison with the trend obtained by choosing the last 10 seconds.

### 3.1.2. Constant heating

The results obtained for the experiments using constant incident heat flux are summarized in Fig. 24 and 25 for visual analysis and last 10 seconds intervals, respectively. They are also summarized in Table 14.

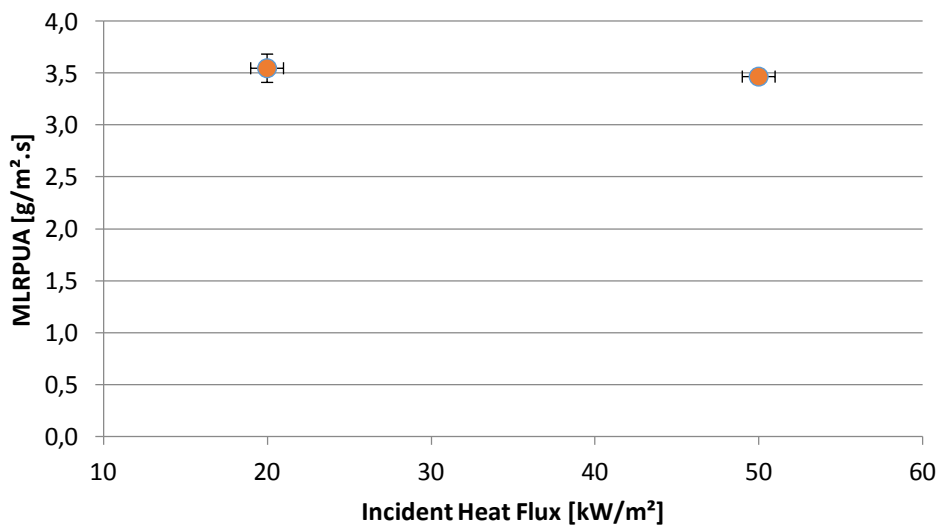


Figure 24 – Average MLR per unit area for the visual analysis as a function of the incident heat flux.

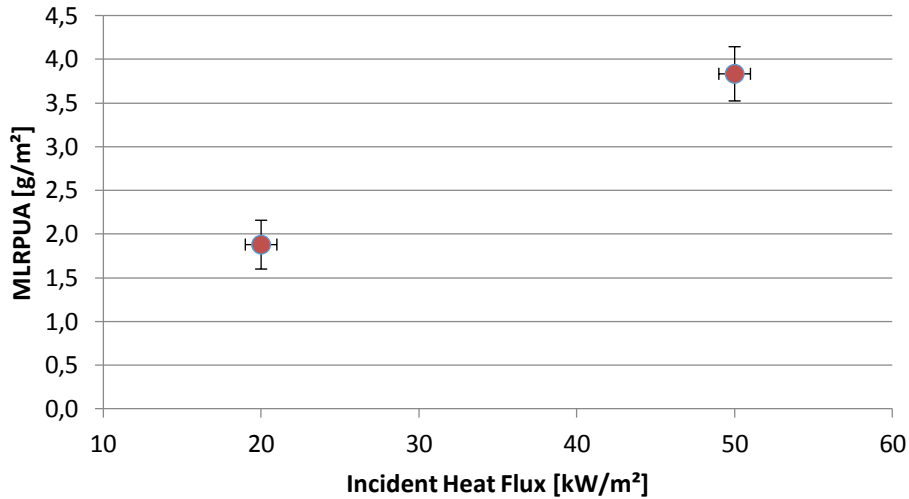


Figure 25 - Average MLR per unit area for the last 10 seconds as a function of the incident heat flux.

Table 14 – Summary of the results obtained for MLRPUA for the visual analysis and last 10 seconds for the samples subjected to constant incident heat flux.

IHF [kW/m <sup>2</sup> ]	Visual analysis (VA)	10 s	Average VA	Error (VA)	Average 10s	Error 10s
20	3,41	1,60	3,55	0,14	1,88	0,28
	3,69	2,16				
50	3,41	4,14	3,47	0,06	3,83	0,31
	3,52	3,52				

By looking again at Table 13, it is possible to observe that the values obtained here are slightly higher than most of the ones reported in the previous works, with the exception of Vermesi *et al.*, which found 4.9 and 5.2 g/m<sup>2</sup>.s. Also, as illustrated in Fig. 11, most values reported in the literature are between 1 and 2.5 g/m<sup>2</sup>.

The same explanation provided in 3.1.1 about the uncertainties is valid here.

### 3.2. Temperature Experiments

In this section, the temperature distribution within the fuel is discussed. This thermal gradient impacts directly the measurement of the surface temperature, since it is not measured directly, but through a mathematical fit that described this distribution.

The results for transient and constant heat fluxes are discussed separately in this section and compared to previous works.



### 3.2.1. Temperature distribution within the solid fuel

As discussed in 2.5.1, a quadratic fit was chosen in order to estimate the surface temperature. This fit was the one that provided the best accuracy in terms of the  $R^2$ . Fig. 26 depicts the temperature distribution with the depth for sample T-60-1-T.

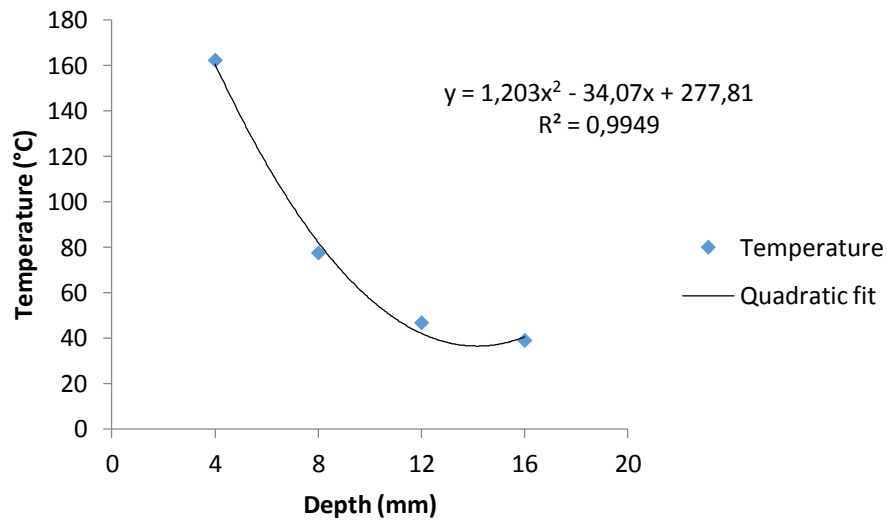


Figure 26 – Temperature distribution with depth in the sample T-60-1-T.

This result shows the steep increase in the temperature near the surface. Figure 27 shows the temperature increase with time for the different depths for the same sample, which is subjected to a heating rate of  $60 \text{ W/m}^2\cdot\text{s}$ .

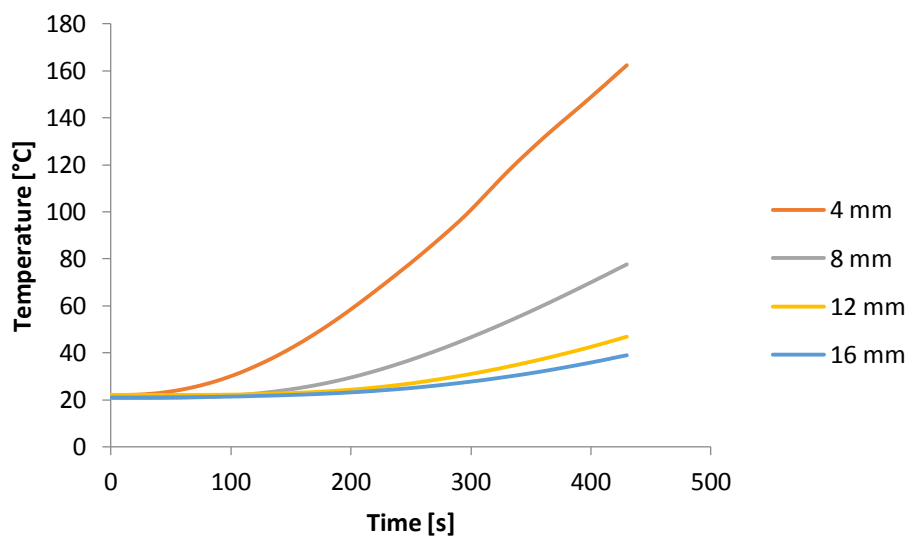


Figure 27 – Temperature evolution with time at all depths studied (4, 8, 12 and 16 mm). Sample T-60-1-T.

These results reflect the difficulty in estimating the surface temperature with an extrapolation methodology. Near the surface, temperature changes significantly, so any uncertainty associated to a mathematical fit or thermocouple position will affect significantly the results.

### 3.2.2. Transient heating

The temperature experiments show an increase in the surface temperature with the heating rate, as illustrated in Fig. 28. The results are also summarized in Table 15, which shows the average temperature and the difference between the average and the maximum (Error +) and the minimum (Error -) values for each heating rate.

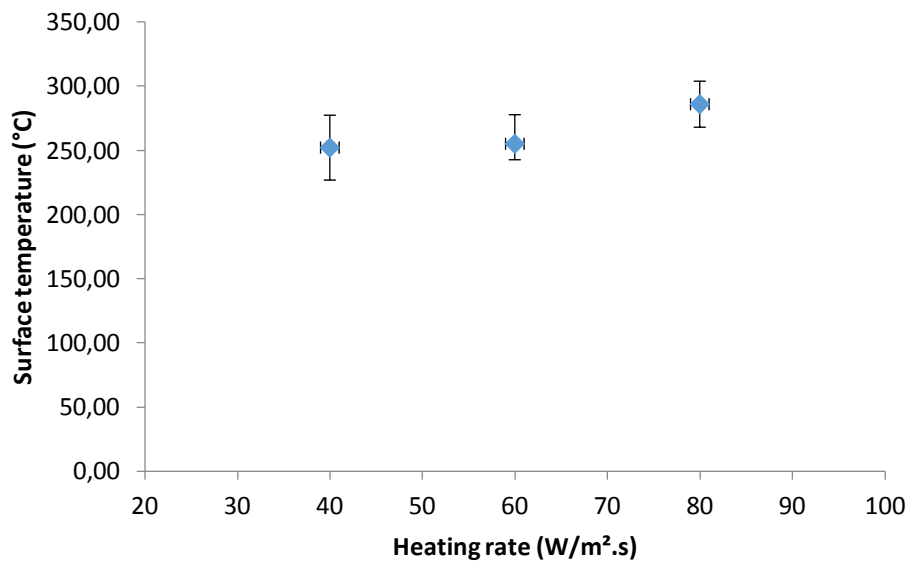


Figure 28 – Surface temperature as a function of the heating rate.

Table 15 – Summarized results of average surface temperature and the difference between the maximum and minimum values obtained (Error + and Error -, respectively).

IHF	Average Temperature	Error +	Error -
40	252,17	25,26	25,26
60	255,12	22,69	12,42
80	286,01	17,94	17,94

Rhodes reported a similar behaviour in the trend, even though in their work a constant incident heat flux was used. It was observed an increase in the surface temperature with the incident heat flux. Although the boundary conditions are different (transient or

constant incident heat fluxes), the comparison is done by assuming that both cases imply that heating occur faster for higher constant incident heat fluxes and higher heating rates, and what mostly influences the heat transfer process is not the total amount of energy, but the rate at which this energy is provided [6].

Although the influence of bubbling phenomenon is still not very well understood, it is suggested that the bubbles lead to lower surface temperatures [10]. In the lower heating rates, bubbling phenomena was much more significant than in higher heating rates, as will be discussed in 533.4. This explains the increase in the temperature with the heating rate.

However, in lower depths it was observe a decrease in the temperature with the heating rate, except for the depth of 4 mm, where a decrease occurred in the heating rate of 60  $W/m^2$ , but was followed by an increase at 80  $W/m^2$ , as showed in Fig. 29.

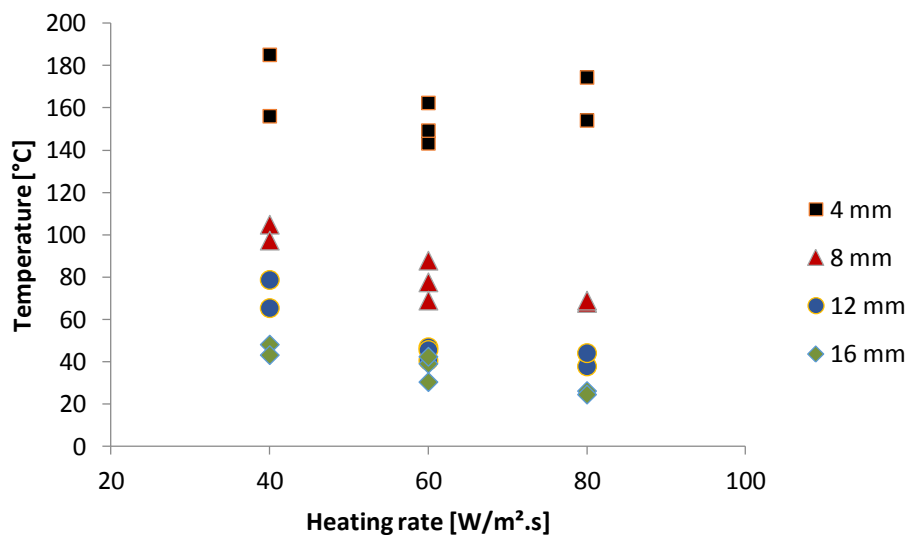


Figure 29 – Temperature at the depths of 4, 8, 12 and 16 mm as a function of the heating rate.

This qualitative difference in the results reflects the uncertainties related to the experiment, since the same trend would be expected to occur if a mathematical fit is used, i.e. if the temperature decreases with the heating rate at 8 mm, it should also increase at the surface.

Bubbling and melting phenomena play a role only at the surface, and therefore in reality the surface temperature variation with the heating rate can have a different trend than in inner depths. However, the mathematical fit does not comprise these phenomena.

These differences are explained by the uncertainties associated to the methodology adopted. Firstly, the uncertainty in the quadratic fit which is an approximation taken with the temperature measurements and therefore involve errors. Another uncertainty that plays a role is the position of the thermocouples, which varies slightly from one sample to another, even though the process of drilling them was performed carefully. As explained in 3.2.1, near the surface the thermal gradient is very steep, so any slight difference might influence the final result.

The temperatures found in the present work are lower than the ones reported in previous works. Table 16 summarizes the results from the literature and the present work.

Table 16 – Summary of surface temperature results from literature and present work.

<b>Author</b>	<b>Condition</b>	<b>T<sub>ig</sub> [°C]</b>
Vermesi <i>et al.</i>	20 kW/m <sup>2</sup>	320
Tewarson <i>et al.</i>	-	382
SFPE Handbook	-	378
Lyon <i>et al.</i>	-	304
Lyon <i>et al.</i>	-	280 - 320
Rhodes	19 kW/m <sup>2</sup>	265
Present work	40 W/m <sup>2</sup> .s	252,17
Present work	60 W/m <sup>2</sup> .s	255,12
Present work	80 W/m <sup>2</sup> .s	286,01

As observed in 3.2.1, the temperature increases much faster near the surface, and gradients are much steeper. The quadratic fit underestimates the surface temperature. Moreover, there are also uncertainties related to the position and diameter of the thermocouples. For lower depths, this uncertainty does not affect significantly the results, since the thermal gradients are not very steep. However, near the surface the influence of this uncertainty is much more critical. If the thermocouple at 4 mm is placed slightly lower, it will provide much lower surface temperatures.

### 3.2.3. Constant heating

As showed in Fig. 30 and 31, the temperatures were very low for the 50 kW/m<sup>2</sup> cases. This is due to the fact that, since ignition occurred very rapidly, thermal penetration was very little, and therefore the energy was mostly concentrated in the solid surface. Especially for high incident heat fluxes and heating rates, thermal gradients are expected to be very steep near the surface, and therefore the thermocouple position and thermal inertia influences extremely the results. In this case, the methodology adopted, i.e. thermocouple positions and quadratic fit cannot be applied. The graph represented in Fig. 32 shows a steep increase in temperature at a depth of 4mm, but almost no increase further deep in the solid sample.

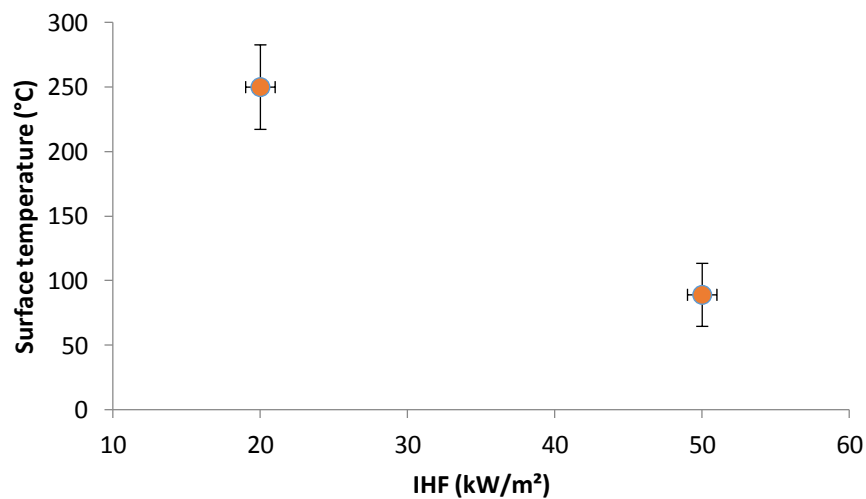


Figure 30 – Surface temperature as a function of the incident heat flux.

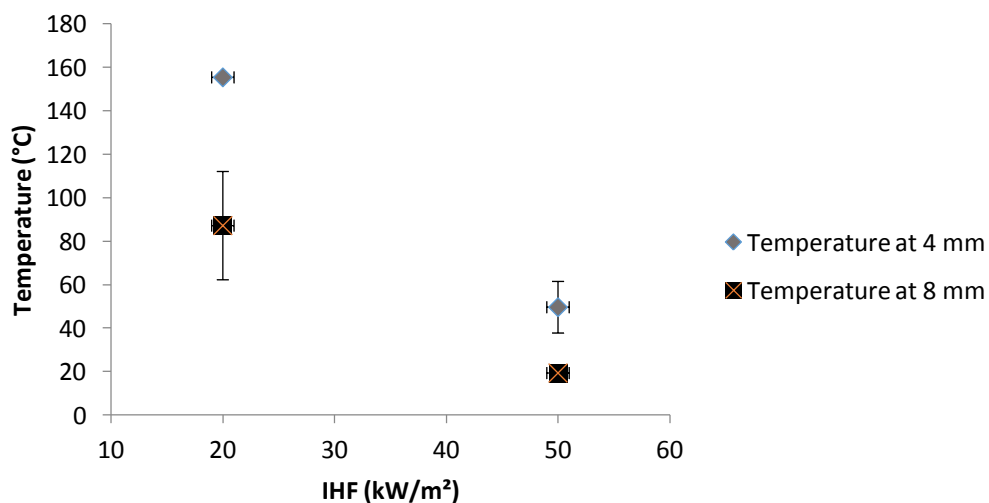


Figure 31 – Temperatures at 4 and 8 mm as a function of the incident heat flux.

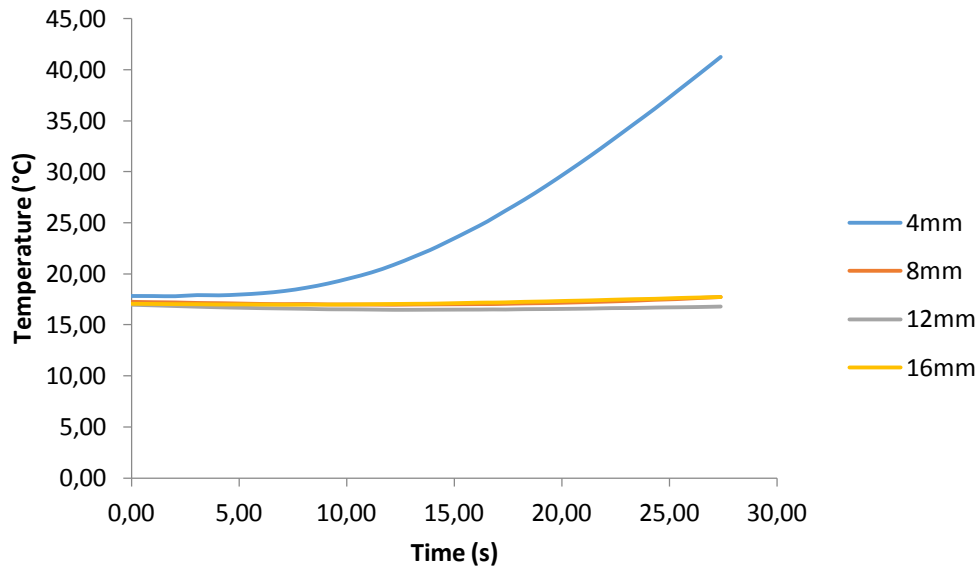


Figure 32 – Temperature evolution with time at different depths for a PMMA sample subjected to a constant incident heat flux of  $50 \text{ kW/m}^2$ .

Here the results obtained for surface temperature were also lower than the ones reported in the literature. Since the value found for the experiments using  $50 \text{ kW/m}^2$  are unreasonable, it was not compared here. This comparison is summarized in Table 17.

Table 17 – Comparison of the results obtained in the present work and previous works.

Author	Condition	$T_{ig}$ [°C]
Vermesi <i>et al.</i>	$20 \text{ kW/m}^2$	320
Rhodes	$19 \text{ kW/m}^2$	265
Present work	$20 \text{ kW/m}^2$	250.05

Different methods for measuring the surface temperature are normally utilized. This leads to a difficulty in the comparison, since the results are affected by different uncertainties.

Also, the explanation related to the uncertainties in 3.2.2 is also applicable here.

#### 3.2.4. Conductive heat losses

As mentioned in 2.5.2, it was assumed that conductive losses take place at the back surface at the material, and it is measured with the thermocouple at the aluminium

block. The results are represented graphically in Fig. 33 and 34 for the transient and constant heat flux experiments, respectively.

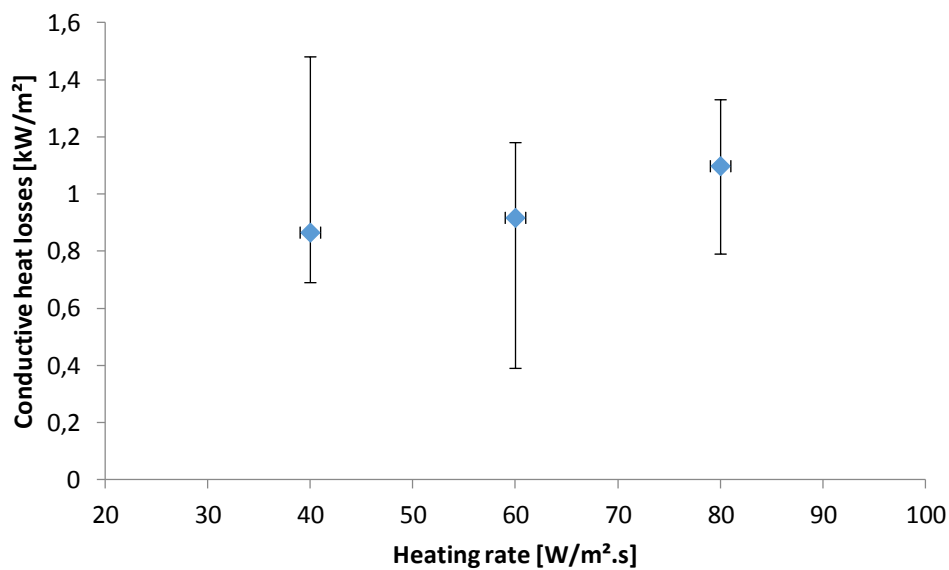


Figure 33 – Average of the conductive heat losses as a function of the heating rate for the transient heating case.

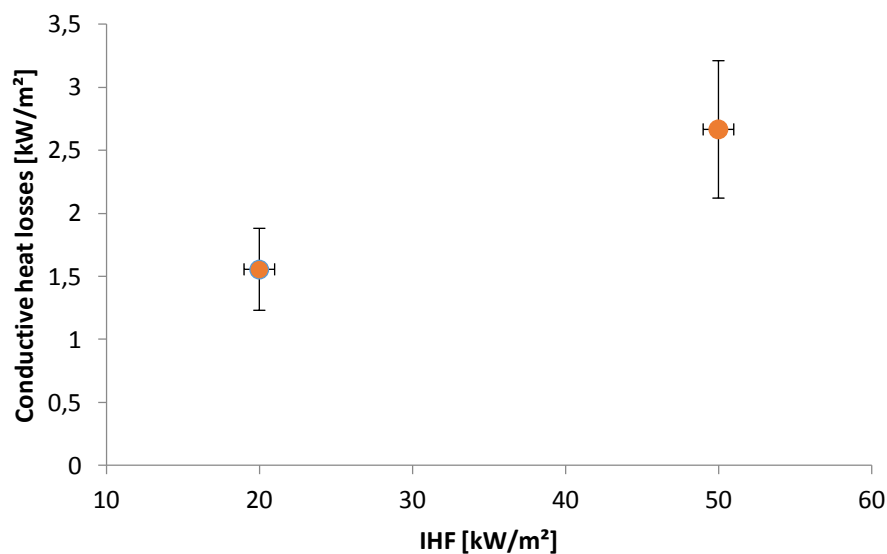


Figure 34 – Average of the conductive heat losses as a function of the incident heat flux for the constant heating case.

A great deviation between the values was observed, as represented with the error bars. This is due to the fact that the temperatures in the aluminium block did not change significantly, so any small increase influences the final result significantly. Moreover, in some experiments it was observed a drop in the temperature, followed by an increase,

as depicted in Fig. 35. A possible reason for that is the inlet flow of air, which probably cooled down the aluminium block in the beginning of the experiment.

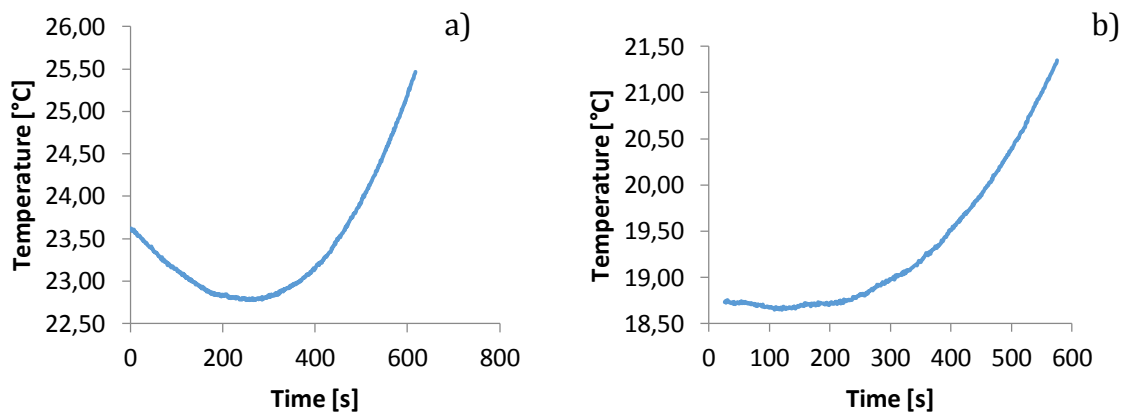


Figure 35 – Temperature variation with time in the aluminium block for samples a) T-40-3-T and b) T-40-1-T.

Considering that the error was too high in the transient heat flux experiments, it is not possible to state there is an actual increase in the conductive losses with the heating rate, as shown by the average values in Fig. 33.

For the experiments using constant incident heat flux, an increase in the conductive heat losses was observed. This trend is not in accordance with the results reported by Santamaria *et al.*, which observed a decrease in the conductive losses with the heating rate [10]. Also, as discussed in 3.2.3, the thermal penetration in the samples subjected to an IHF of  $50 \text{ kW/m}^2$  was very low, so the conductive heat losses were expected to be also very small. In this case, the uncertainties influenced significantly the results. Since the calculation is based on a temperature difference between each data point and only the value of the conductive heat loss at ignition is considered, the result becomes very vulnerable to the influences of uncertainties. In other words, if by any change an error in the measurement occurs at ignition, it will influence directly the result, whereas in results based on an average the other values offset the error. Also, the thermal inertia of the thermocouple plays an important role here.

The values of the conductive heat losses are shown individually for each heating rate in Table 18, with the respective uncertainties calculated as explained in 2.6. These uncertainties associated to the measurements are very little and, therefore, are not visible in graphs.



Table 18 – Conductive heat losses and the respective uncertainty for each experiment.

HR [W/m <sup>2</sup> .s]	Sample name	Cond. Losses	Uncertainty
40	T-40-1-T	1.48	0.00363
	T-40-2-T	0.69	0.00967
	T-40-3-T	1.04	0.00848
60	T-60-1-T	1.18	0.00789
	T-60-2-T	0.39	0.00643
	T-60-3-T	1.18	0.00581
80	T-80-2-T	1.18	0.00971
	T-80-3-T	0.79	0.00914
	T-80-4-T	1.09	0.00944
	T-80-5-T	1.33	0.00927

These results show that the final result is not significantly affected by the uncertainties associated to the dimensions, the specific heat and the mass of the aluminium block.

### 3.2.5. Radiative and convective heat losses

The radiative and convective losses take place at the front surface of the solid sample, which is exposed to the irradiation. In the transient case, the heat losses are nearly constant with the heating rate. However, by using a constant heating the losses increased significantly with the HR. Both cases are represented in Figs. 36 and 37.

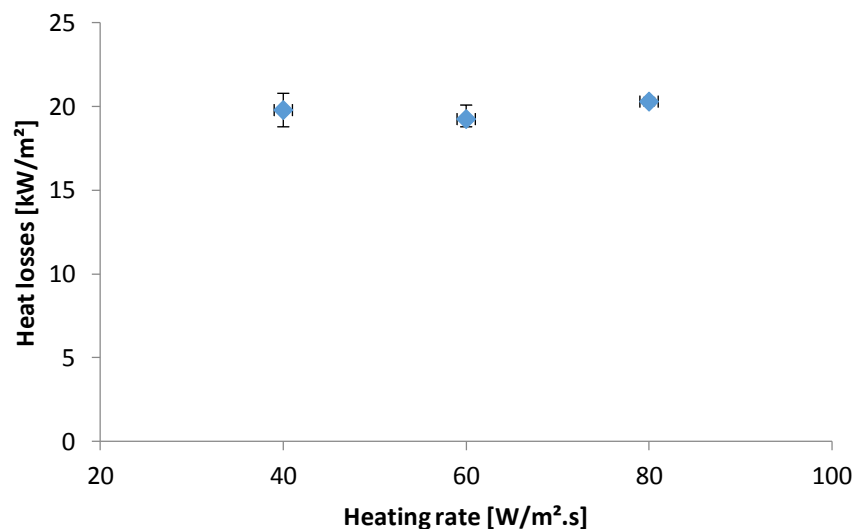


Figure 36 – Radiative and convective heat losses at the exposed surface as a function of the heating rate.

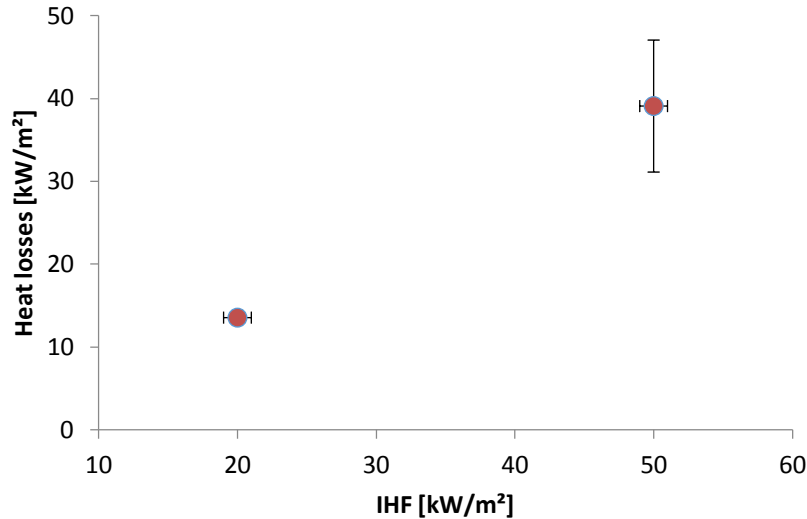


Figure 37 - Radiative and convective heat losses at the exposed surface as a function of the incident heat flux.

Santamaria *et al.* reported an increase of the surface heat losses with the heating rate. However, they used samples of PA6 [10].

The parameters that influence the surface losses are the flow characteristics at the surface and the pilot location, which is related to the convective loss, the surface temperature, which is related to both reradiation and convection, and the absorptivity of the PMMA, which affects reradiation [10].

Since the NHF and the IHF at ignition increase with temperature, the surface losses will also increase (see 2.5.2).

### 3.2.6. Net heat flux (NHF)

The net heat flux is the energy absorbed by the sample, and therefore is the responsible for the surface heating and the pyrolysis process. This parameter is directly dependent on the absorptivity of the material [14].

As illustrated in Fig. 38, the neat heat flux increases with the heating rate. This results is not in accordance qualitatively with the observations of Santamaria *et al.*, where the NHF did not change significantly with the heating rate.

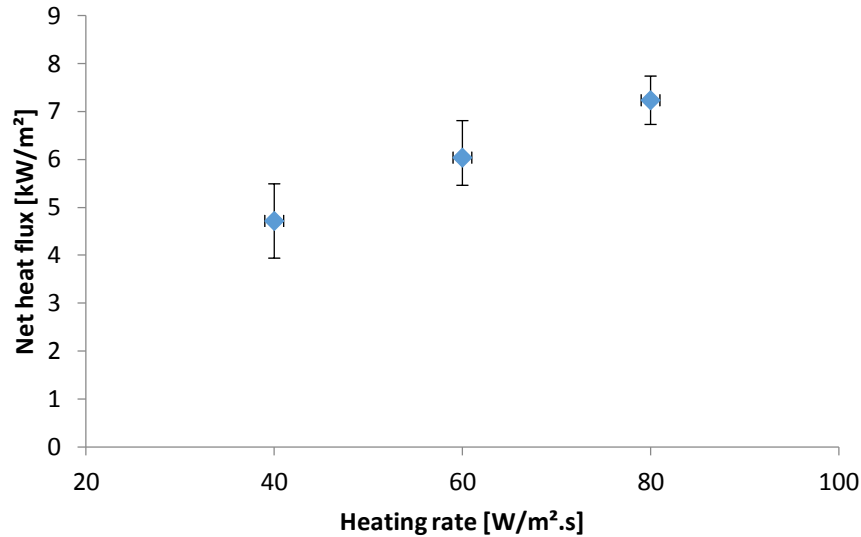


Figure 38 – Net heat flux as a function of the heating rate for the experiments under transient irradiation.

A higher NHF will lead to higher surface temperatures, and therefore to higher volatilization. As reported in 3.2.2, the surface temperatures indeed increased with the heating rates.

In the case of constant incident heat flux of 20 kW/m<sup>2</sup>, a maximum value of 6.91 kW/m<sup>2</sup> and a minimum of 5.98 kW/m<sup>2</sup> were found. However, for the IHF of 50 kW/m<sup>2</sup> unreasonable values were found – maximum of 18.87 kW/m<sup>2</sup> and minimum of 2.94 kW/m<sup>2</sup>. Therefore, the results are not shown graphically. Again, this reflects the issue when applying the quadratic fit for a high heating rate. Since inconsistent data was obtained for the temperatures in these experiments due to the lack of thermal penetration, as explained in 3.2.3, the results obtained for this IHF are neglected.

### 3.3. Incident heat flux at ignition and ignition delay time

It was observed an increase in the critical incident heat flux at ignition with increasing heating rate, whereas the time to ignition decreased. The results are summarized graphically in Fig. 39.

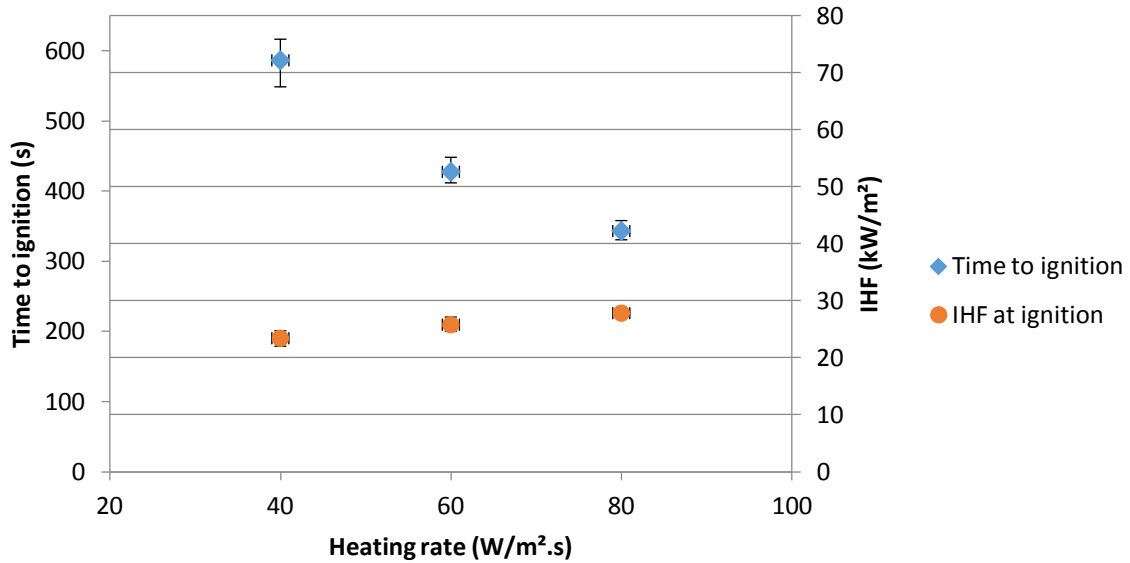


Figure 39 – Time to ignition and incident heat flux at ignition for the three different heating rates.

This increase in the incident heat flux at ignition can be explained by the fact that, in higher heating rates, the surface heat losses are expected to be higher. This means that the net heat flux will be lower, and therefore less energy is supplied to volatilization. The volatiles are pyrolysis products, and therefore their release is controlled by the heat transfer in the solid.

These values are, however, higher than the critical heat flux of PMMA in constant heating conditions. For instance, ignition occurred in the samples exposed to 20 kW/m<sup>2</sup>, but no ignition occurred at an IHF of 20 kW/m<sup>2</sup> in the transient cases. This is due to the fact that, in experiment using constant heating, energy is supplied in the same rate from the beginning of the test, whereas in transient cases this rate of energy supply increases with time. Also, due to the thermal inertia of the material, the response of the solid to the incident heat flux is not instantaneous [9]. Pyrolysis is controlled by the thermal gradient in the solid, and this gradient depends on the energy absorbed [10].

The ignition delay time obtained in this thesis is in great accordance with previous results reported in the literature, as shown in Fig. 40.

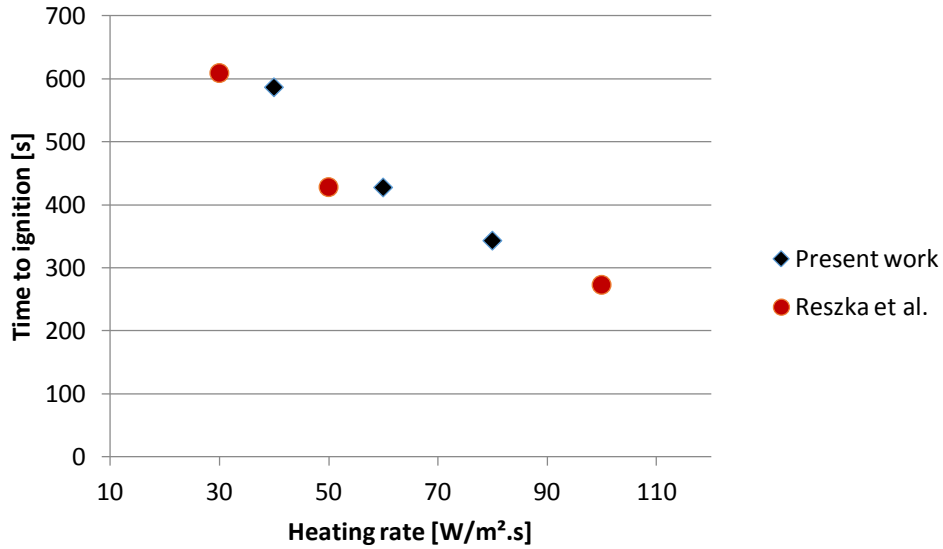


Figure 40 – Time to ignition vs. Heating rate for the present work and value from literature [5].

The same behaviour was observed by Santamaria *et al.*, where PA6 samples were subjected to transient incident heat fluxes. As discussed in 1.3.6, the time to ignition decreased with the heating rate, whereas the incident heat flux at ignition increased with the HR.

The results obtained for the constant incident heat flux are represented in Fig. 41.

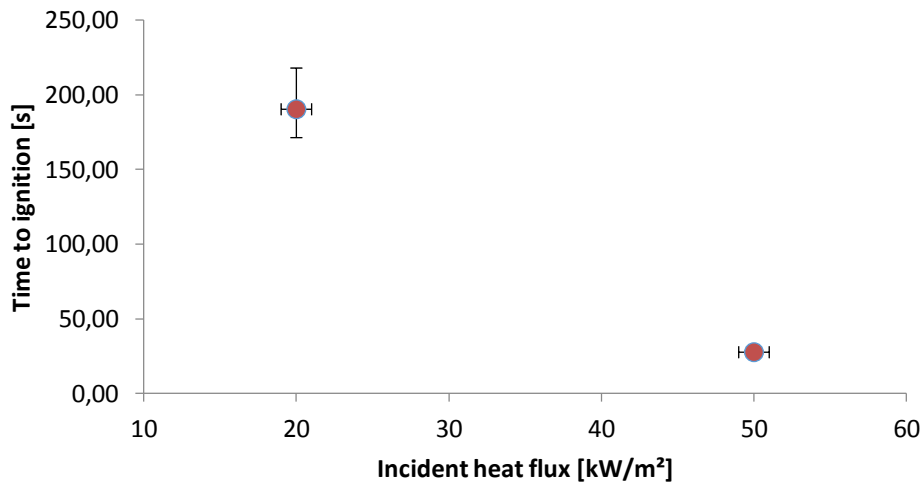


Figure 41 – Time to ignition as a function of the incident heat flux for the constant heating case.

The comparison with previous results is presented in Table 19 and Fig. 42.

Table 19 – Comparison between results obtained by Rhodes [17] and the present work.

Author	IHF (kW/m <sup>2</sup> )	t <sub>ig</sub> (s)
Rhodes	19	141
		135
	50	20
		25
		26
Present work	20	190.38
	50	27.63

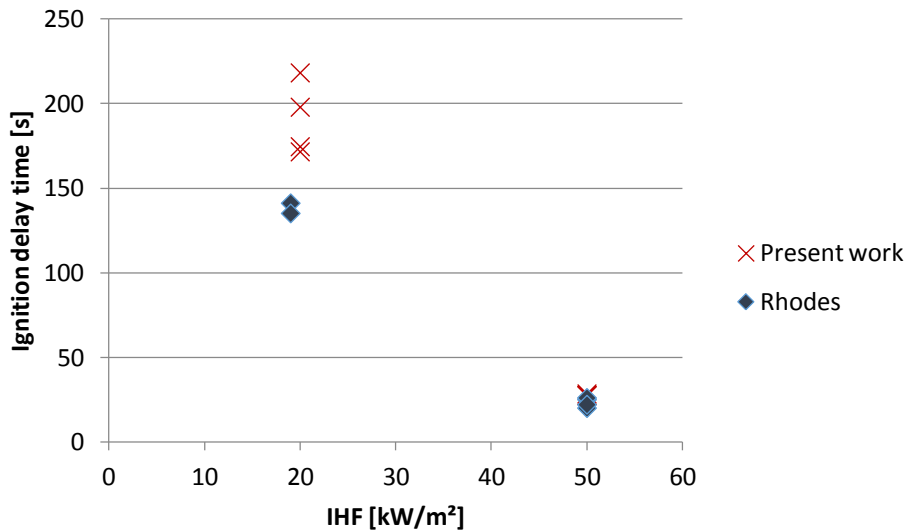


Figure 42 – Ignition delay time as a function of the IHF for the present work and results obtained by Rhodes [17].

The results are in great accordance with previous literature for the IHF of 50 kW/m<sup>2</sup>, but are higher for the IHF of 20 kW/m<sup>2</sup>.

### 3.4. Bubble formation

A phenomenon observed visually during the experiments was the bubbling formation. This leads to an acceleration in the onset of ignition due to the fact that the bubbles cause a reduction in the thermal inertia of the material [3].

It was observed that, for lower heating rates, bubbles were larger and their formation lasted longer. In the case of higher heating rates, bubbles were much smaller and, as soon as they started to form, ignition was achieved. Fig. 43, 44 and 45 show screenshots from the experiments recordings. They were taken at approximately 1 second before the first flame appeared.

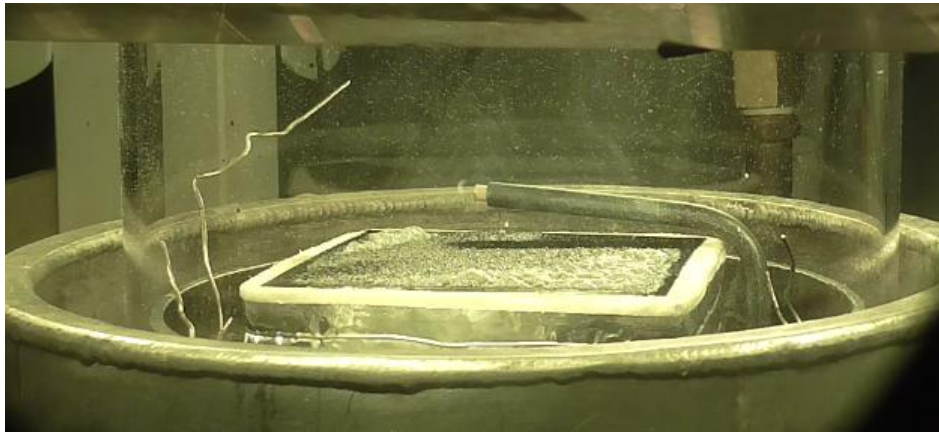


Figure 43 - Bubbling formation in a PMMA sample subjected to a heating rate of  $40 \text{ W/m}^2\cdot\text{s}$ .

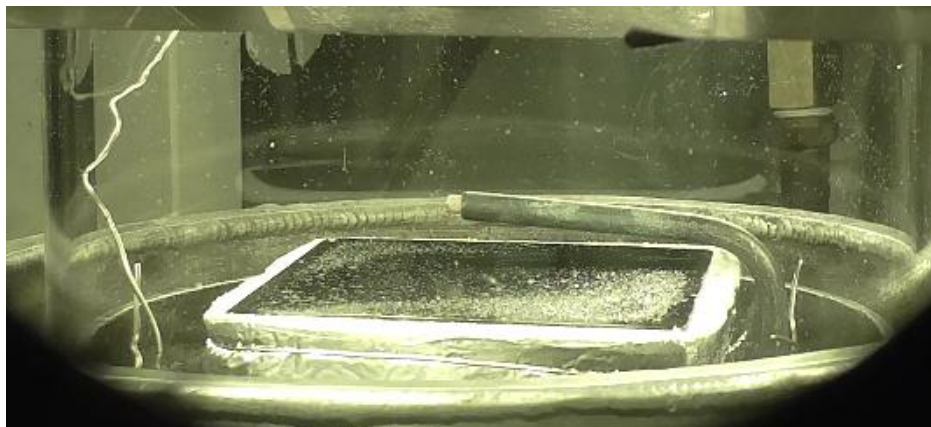


Figure 44 - Bubbling formation in a PMMA sample subjected to a heating rate of  $60 \text{ W/m}^2\cdot\text{s}$ .

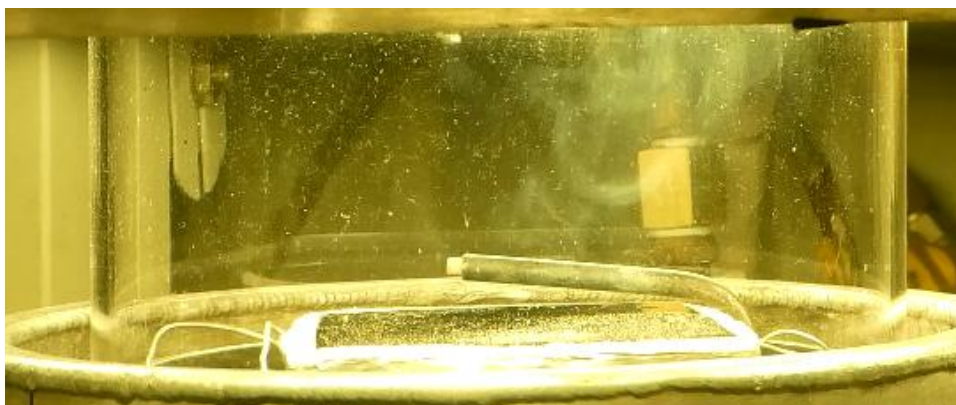


Figure 45 - Bubbling formation in a PMMA sample subjected to a heating rate of  $80 \text{ W/m}^2\cdot\text{s}$ .

This can be explained by the fact that, in higher heating rates, the surface heats up faster and most of the energy remains contained in the surface, instead of permeating in the solid. When the heating rate is lower, the energy that reaches the surface is conducted through the sample, and therefore smaller gradients are expected. The steeper thermal gradient leads to a lower bulk kinematic viscosity, which allows an easier migration of bubbles through the solid sample and, therefore, a higher amount of them reaches the surface more quickly [7].

Bubbling formation was studied by Kashiwagi [13], and the same trend was observed. For lower incident heat fluxes, bubbling played a significant role, whereas in higher incident heat flux scenarios ignition occurred when the bubbling process started to develop and bubbles were much smaller.

As mentioned in 3.1 and 3.2, the bubbles play an important role in the ignition conditions, since it affects the heat transfer in the material and, therefore, the pyrolysis rate [10].

### **3.5. Limitations and source of errors**

- Type of equipment

The type of equipment affects directly the results. This is due to the source of ignition (electrical spark, pilot flame, and so on) and the heating source (e.g. infrared lamps) [3]. For instance, the pilot flame provides a more uniform heat over the sample surface due to the fact that it is larger than the spark, whereas the electrical spark is more punctual. It means that, if a mixture reaches the LFL at a certain distance from the hot spot, it might ignite in the presence of a pilot flame, but not in the presence of an electrical spark.

Moreover, according to Janssens the use of a pilot flame increases the heat transfer to the sample [3].

- Sample preparation

There are always small uncertainties related to sample preparation. Firstly, the measures considered are 85 x 85 x 25 mm. However, small differences in the dimensions will occur. Moreover, in the temperature experiments part of the sample was not covered with the insulation paper in order to allow space for the



thermocouples. This will lead to small heat losses through the lateral surface, where no insulation paper is provided.

- Thermocouples

Near the surface, the thermal gradient is extremely steep. Therefore, small deviation in the thermocouple position can play a significant role, and also the thermocouple diameter. Moreover, the thermal inertia of the thermocouples leads to a delay in the measurement. In other words, if the temperature is increasing, the value indicated by the thermocouple is actually slightly lower than the real temperature.

- Configuration of the pilot flame

The pilot flame must be positioned at 10 mm from the horizontal surface and 10 mm from the side of the sample. Moreover, it must have a length of 10 mm. However, there is an inherent error associated to this measurements, which means that the pilot flame was lower in some experiments than in others, and also had slightly different lengths.

- Mathematical fit

The quadratic fit was chosen due to the fact that it was the one providing the best approximation, i.e. the highest  $R^2$  value and therefore it is assumed to be the most suitable to describe the temperature distribution within the solid. However, other mathematical fits could also be chosen, such as the exponential one, and it is not necessarily true that the thermal gradient will be quadratic. Moreover, there are uncertainties related to the approximation itself. The  $R^2$  never equals one, which means that there is a deviation between the value predicted by the fit and the real value.

- One-dimensional heat transfer assumption

As aforementioned, it was assumed that heat transfer is one-dimensional, which means that energy permeates uniformly through the whole thickness of the sample. However, in reality the heat transfer phenomenon is much more complex. At the same depth, the heat flux, temperature and also thermal conductivity can be different.

- Assumption of inert solid until ignition

In the classic ignition theory, all the processes occurring prior to ignition, i.e. related to pyrolysis, are neglected and the solid is assumed to be inert until ignition is achieved.

However, this does not represent reality, since all this degradation that the material undergoes leads to ignition due to the volatilization. This assumption can lead to an underestimation of ignition delay times and inaccurate surface temperatures [3,19].

- Assumption that thermal and material properties are constant with temperature

It was assumed that the thermal conductivity, density and specific heat are independent of the temperature. However, in reality they vary with temperature. This affects directly the neat heat flux, which involves the thermal conductivity of the PMMA. It also affects the results for conductive heat losses in the aluminium block, since the calculations involve the specific heat. However, for the latter case the increase in the temperature is low, so the effects on the thermal property are not significant.

- Assumption of heat losses only in the surfaces

As aforementioned, it was assumed that all heat losses occur at the front surface (radiative and convective losses) and through the back of the sample (conductive losses to the aluminium block). However, minor losses also occur through the insulation. Moreover, as mentioned above part of the samples used for temperature experiments was not covered, so the thermocouples can be placed.

- Uncertainty associated to the interval choice for the MLR calculation

As stated in 3.1.1, the interval choice in the Mass vs. Time graph affects significantly the results of MLR. The graphs present in that section show quantitative and qualitative differences between the visual observation and last 10 seconds.



## CHAPTER 4

### CONCLUSION

In the present work, the ignition of PMMA under transient incident heat fluxes was studied. The parameters assessed were mass loss rate, surface temperature, ignition delay time, conductive heat losses through the back surface of the material and radiative and convective heat losses at the surface exposed to the incident heat flux.

Samples were exposed to heating rates of 40, 60 and 80 W/m<sup>2</sup> in the Fire Propagation Apparatus (FPA). Experiments using constant incident heat flux (20 and 50 kW/m<sup>2</sup>) were also carried out in order to compare with previous works, since most of them deal with constant boundary conditions.

The mass loss rate was found to increase with the heating rate. However, the error was significantly high. The average values were 3.69, 3.83 and 4.06 g/m<sup>2</sup>.s for the heating rates of 40, 60 and 80 W/m<sup>2</sup>.s, respectively. For the heating rate of 40 W/m<sup>2</sup>.s, the maximum value was 4.62 g/m<sup>2</sup>.s and the minimum, 2.93 g/m<sup>2</sup>.s. For the HR of 60 W/m<sup>2</sup>.s, the maximum value was 4.73 g/m<sup>2</sup>.s and the minimum was 2.81 g/m<sup>2</sup>.s. For the HR of 80 W/m<sup>2</sup>.s, the maximum and minimum values were 5.73 and 2.73, respectively.

The highest value observed for mass loss rate was 4.06 g/m<sup>2</sup>.s, which occurred in a sample subjected to a heating rate of 80 W/m<sup>2</sup>.s. The lowest value was 3.69 g/m<sup>2</sup>.s at the heating rate of 40 W/m<sup>2</sup>.s. In the case of constant incident heat flux, a very small difference was observed for the difference incident heat fluxes. The average mass loss rate was 3.51 g/m<sup>2</sup>.s, and the minimum value was 3.41 g/m<sup>2</sup>.s, which was observed in both 20 and 50 kW/m<sup>2</sup> experiments and the maximum was 3.69 g/m<sup>2</sup>.s at the IHF of 20 kW/m<sup>2</sup>.

The maximum value obtained for surface temperature was 303.94°C at the heating rate of 80 W/m<sup>2</sup>.s, whereas the minimum was 226.91°C at the heating rate of 40 W/m<sup>2</sup>.s and at the constant incident heat flux of 20 kW/m<sup>2</sup>.

The temperatures obtained for the incident heat flux of 50 kW/m<sup>2</sup> were extremely low due to the fact that the thermal gradient is very steep, and therefore there is a significant difference between the temperature at 4 mm and the surface temperature.

The net heat flux and the surface losses were found to increase with the heating rate, and an average value of  $6 \text{ kW/m}^2$  was found for the former and  $31.75 \text{ kW/m}^2$  for the latter.

#### **4.1. Recommendation for future work**

As observed in the temperature results, the mathematical fit led to an underestimation of the surface temperature. Therefore, for future work it is recommended to measure directly the surface temperature in order to minimize the uncertainties, although this is a hard experimental method.

Moreover, different mathematical fits can be used, such as an exponential, if the same methodology is applied.

In the present work, only the parameters associated to the solid phase were studied. It is also important to include an analysis of the gas phase, since it is in this phase that combustion takes place.

The influence of bubbling is not very well understood, and very few literature is available on this topic. Therefore, for future works it is recommended a deeper evaluation on how the bubbling and melting phenomena influence ignition and the conditions leading to flaming combustion.

## **ACKNOWLEDGMENTS**

First of all, I would like to thank the IMFSE board for the opportunity to study such a great master program. I deeply appreciate all the dedication coming from each lecturer, for all of them contributed to my achievement. Moreover, the financial support was essential to my studies.

I would like to thank my supervisor Dr. Rory Hadden for all the support given during this semester. Your help, guidance and patience were essential to the development of this thesis. Thank you for being so comprehensive and positive!

I would like to express my deep gratitude to Simon Santamaría. Although you were physically far away from Edinburgh, you were always present, helpful, open and available to support me.

I would like to extend my thanks to Michal Krajovic and Carlos Rávena. All my activities in the lab would not have been the same without your help.

I would like to express my deep gratitude to my family. My parents, Valeriana and Antonio Carlos, my siblings, Vitor and Joana, and my grandmothers, who stood by my side in all moments. Supported my studies, encouraged me to pursuit my dreams and gave me so much support when I was stressed and concerned. Muito obrigada, eu amo vocês!

I would like to thank my friends, for they supported me in all moments, shared good Skype conversations and good moments. Distance was no longer a matter, since you were still very close to me. A special thanks to Rachel, Renata, Mariana, Ellen and Gabriel, that stood by my side in all moments. Obrigada!

I would like to thank my classmates Alejandra, Kunsulu and Mónica for their company and friendship. Meeting you was a really good part of these 4 semesters!

## REFERENCES

- [1] A. Tewarson and S. D. Ogden, "Fire behavior of polymethylmethacrylate," *Combust. Flame*, vol. 89, no. 3–4, pp. 237–259, 1992.
- [2] A. Matala, *Methods and applications of pyrolysis modelling for polymeric materials*. 2013.
- [3] M. J. Hurley *et al.*, "SFPE handbook of fire protection engineering, fifth edition," *SFPE Handb. Fire Prot. Eng. Fifth Ed.*, pp. 1–3493, 2016.
- [4] J. Luche, T. Rogaume, F. Richard, and E. Guillaume, "Characterization of thermal properties and analysis of combustion behavior of PMMA in a cone calorimeter," *Fire Saf. J.*, vol. 46, no. 7, pp. 451–461, 2011.
- [5] P. Reszka, P. Borowiec, T. Steinhaus, and J. L. Torero, "A methodology for the estimation of ignition delay times in forest fire modelling," *Combust. Flame*, vol. 159, no. 12, pp. 3652–3657, 2012.
- [6] I. Vermesi, N. Roenner, P. Pironi, R. M. Hadden, and G. Rein, "Pyrolysis and ignition of a polymer by transient irradiation," *Combust. Flame*, vol. 163, pp. 31–41, 2016.
- [7] I. G. L. Shmue, "Piloted Ignition and Flame Spread Over Clear and Black PMMA Cylinders in Opposed Flows," 2015.
- [8] S. M. Dakka, G. S. Jackson, and J. L. Torero, "Mechanisms controlling the degradation of poly(methyl methacrylate) prior to piloted ignition," *Proc. Combust. Inst.*, vol. 29, no. 1, pp. 281–287, 2002.
- [9] D. Drysdale, *An introduction to fire dynamics*, vol. 10, no. 2. 1986.
- [10] S. Santamaria and R. Hadden, "Experimental investigation on the ignition of solids under transient radiative heat fluxes .," 2017.
- [11] R. T. Long, J. L. Torero, J. G. Quintiere, and A. C. Fernandez-Pello, "Scale and transport considerations on piloted ignition of PMMA," *Fire Saf. Sci.*, pp. 567–578, 2000.
- [12] C. Lautenberger and C. Fernandez-Pello, "Approximate analytical solutions for the transient mass loss rate and piloted ignition time of a radiatively heated solid in the high heat flux limit," *Fire Saf. Sci.*, pp. 445–456, 2005.
- [13] I. T. Review and T. Kashiwagi, "Polymer combustion and flammability - - role of the condensed phase," pp. 1423–1437, 1994.
- [14] N. Bal and G. Rein, "Numerical investigation of the ignition delay time of a translucent solid at high radiant heat fluxes," *Combust. Flame*, vol. 158, no. 6, pp. 1109–1116, 2011.
- [15] S. Fereres, C. Lautenberger, C. Fernandez-Pello, D. Urban, and G. Ruff, "Mass flux at ignition in reduced pressure environments," *Combust. Flame*, vol. 158, no. 7, pp. 1301–1306, 2011.
- [16] R. E. Lyon and J. G. Quintiere, "Criteria for piloted ignition of combustible solids," *Combust. Flame*, vol. 151, no. 4, pp. 551–559, 2007.

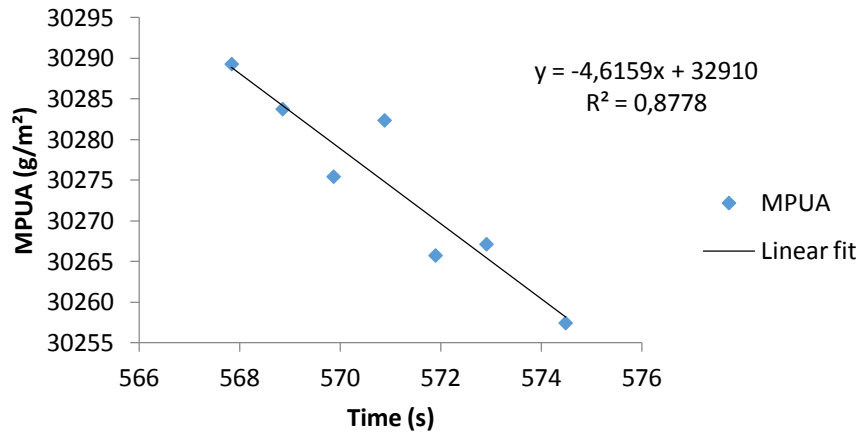
- [17] B. T. R. and J. G. Q, "Burning Rate and Flame Heat Flux for PMMA in a Cone Calorimeter," vol. 26, pp. 221–240, 1996.
- [18] B. T. Rhodes, "Burning rate and flame heat flux for PMMA in a cone calorimeter." University of Maryland, Maryland.
- [19] D. Rich, C. Lautenberger, J. L. Torero, J. G. Quintiere, and C. Fernandez-Pello, "Mass flux of combustible solids at piloted ignition," *Proc. Combust. Inst.*, vol. 31 II, pp. 2653–2660, 2007.
- [20] H. Biteau, A. Fuentes, G. Marlair, S. Brohez, and J. L. Torero, "Ability of the Fire Propagation Apparatus to characterise the heat release rate of energetic materials," *J. Hazard. Mater.*, vol. 166, no. 2–3, pp. 916–924, 2009.
- [21] ASTM International, "ASTM E2058-13a Standard Test Methods for Measurement of Material Flammability Using a Fire Propagation Apparatus (FPA)," vol. i, pp. 1–30, 2013.
- [22] N. A. D. Patricia A. Beaulieu, "Flammability characteristics at applied heat flux levels up to 200 kW/m<sup>2</sup>," *FIRE Mater.*, no. 23 May 2007, p. 4B, 2007.



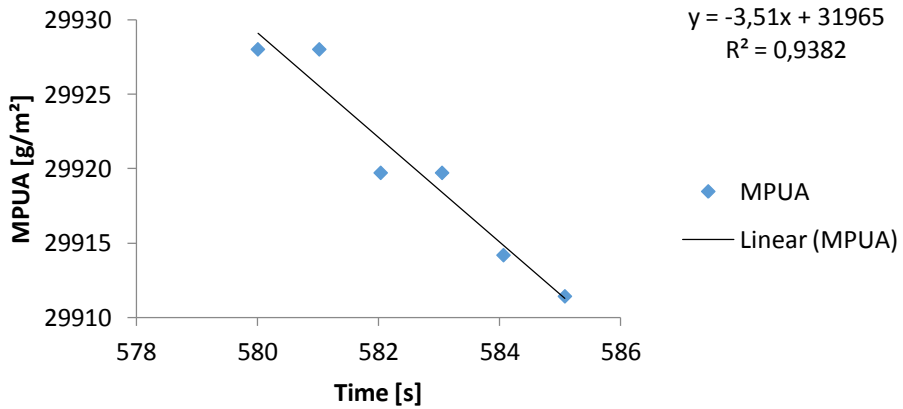
# Appendix I

## Mass loss rate graphs

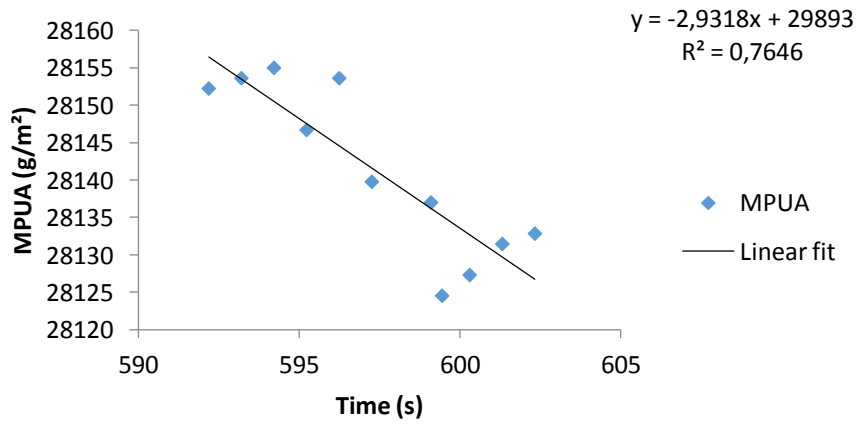
### T-40-1-M



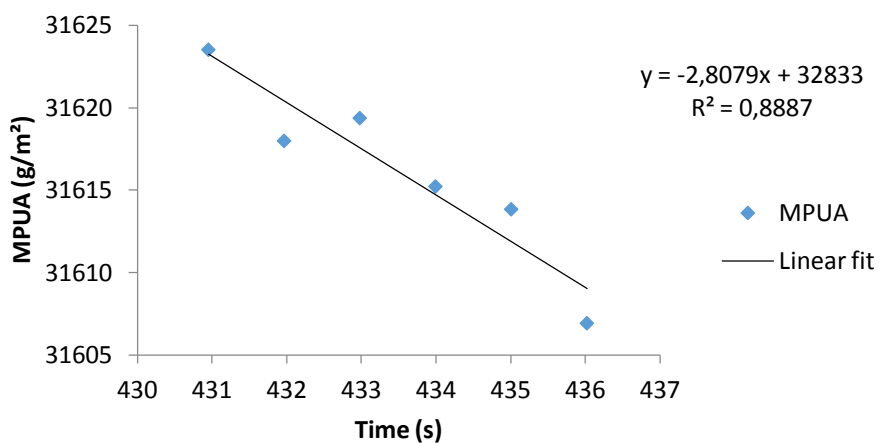
### T-40-2-M



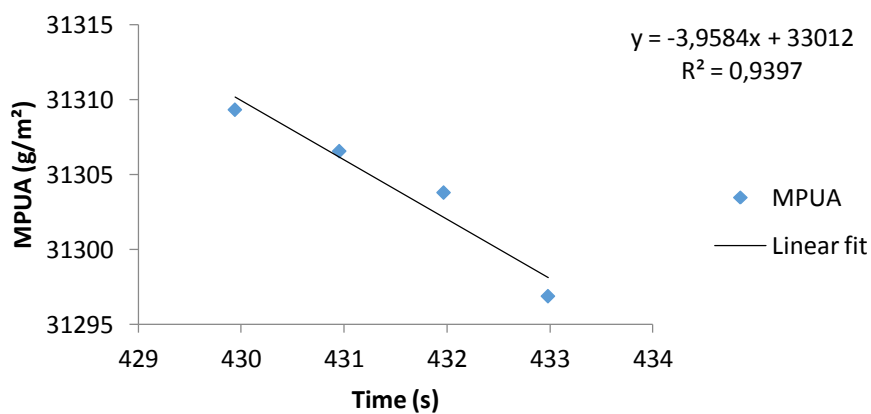
### T-40-3-M



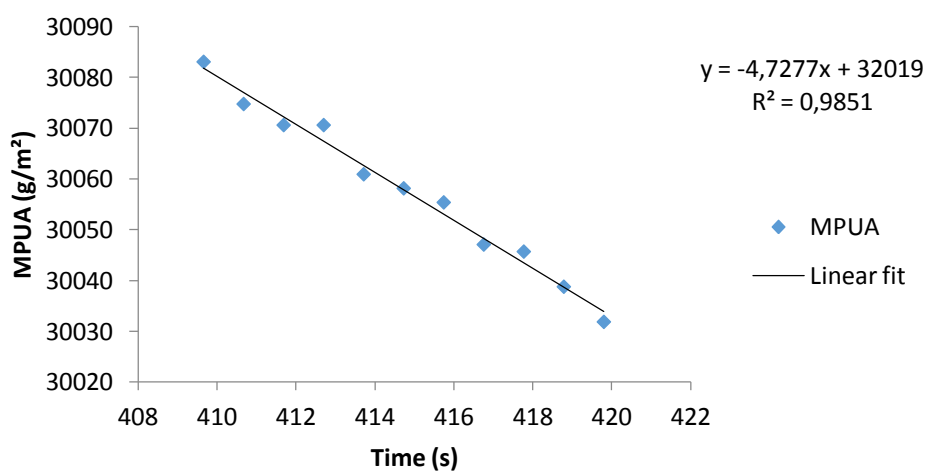
### T-60-3-M



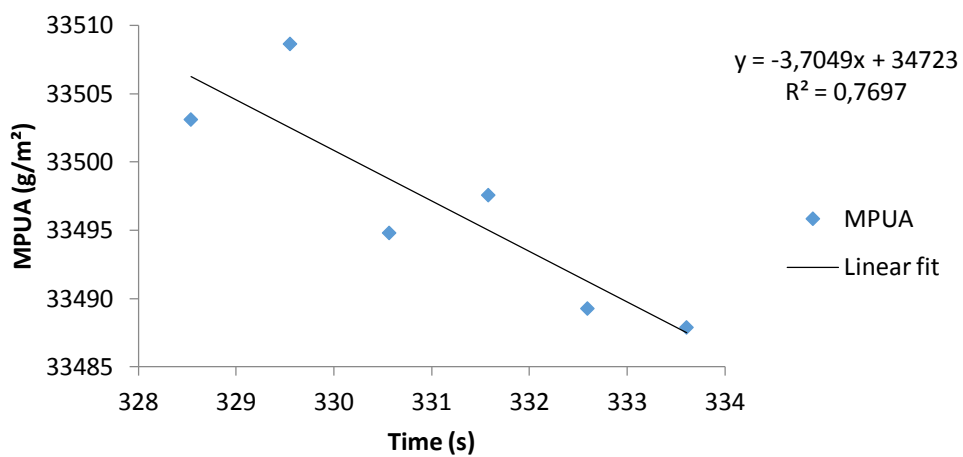
### T-60-4-M



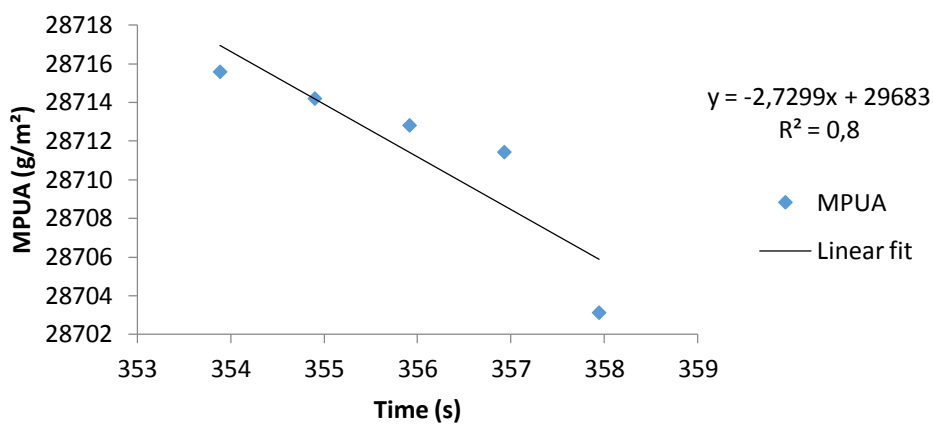
### T-60-6-T



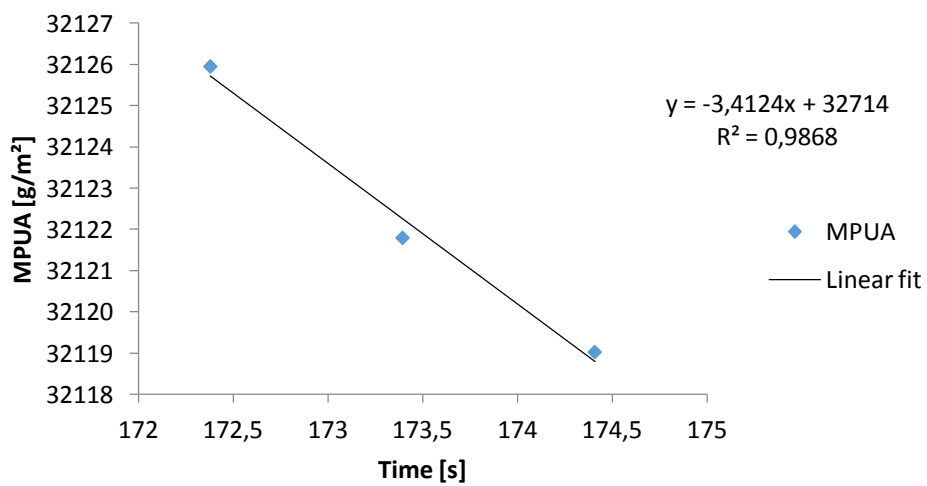
### T-80-1-M



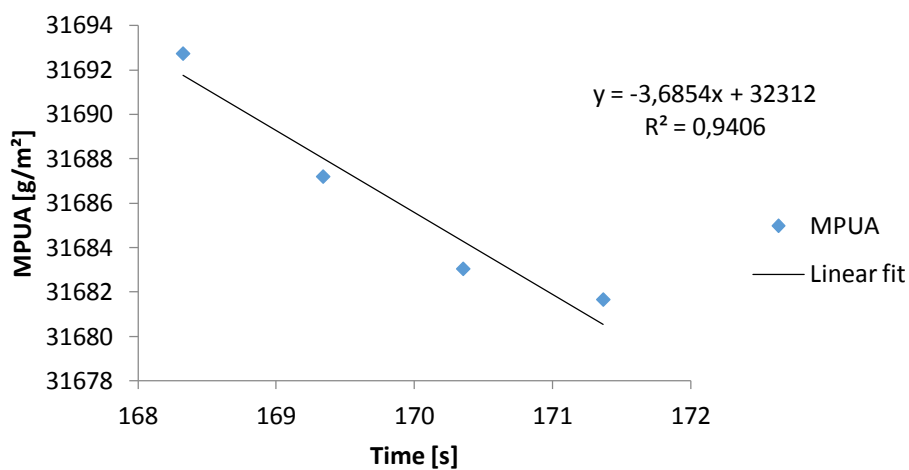
### T-80-4-M



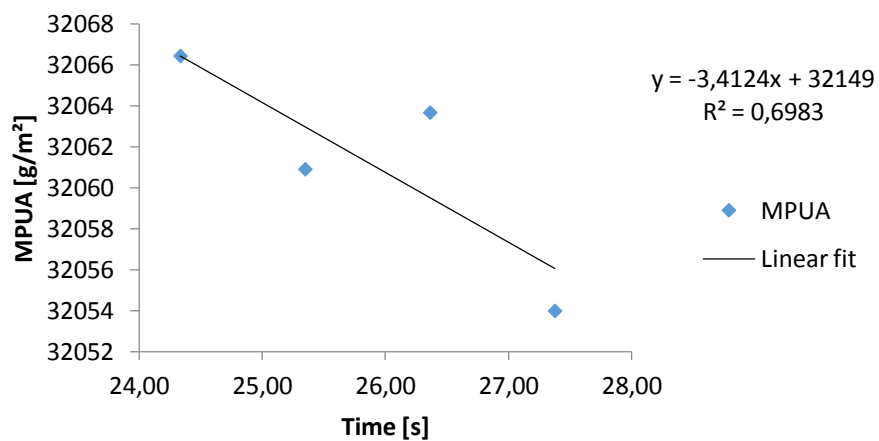
### C-20-1-M



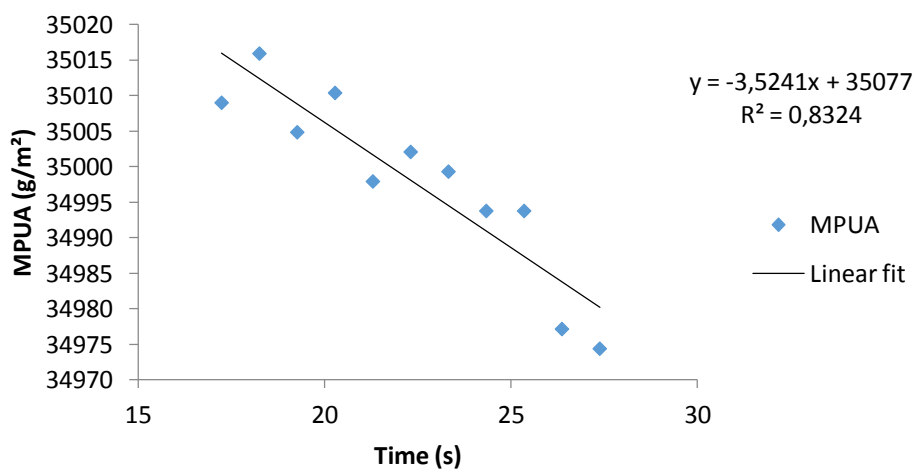
### C-20-2-M



### C-50-1-M



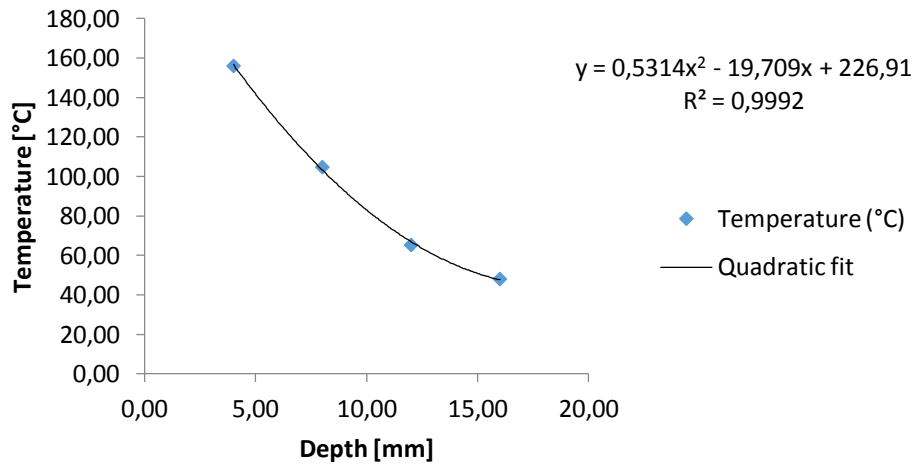
### C-50-2-M



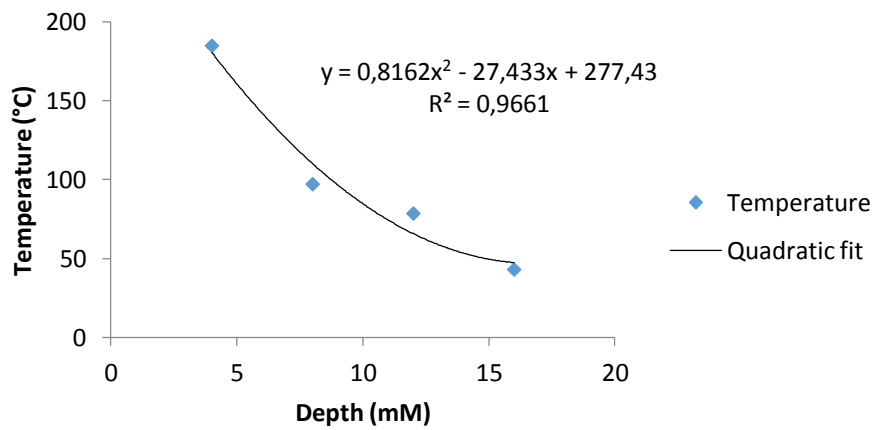
## Appendix II

### Temperature distribution in the solid

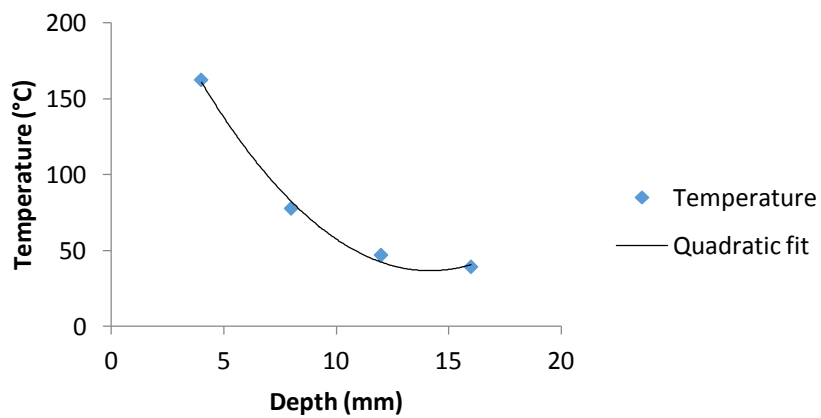
#### T-40-1-T



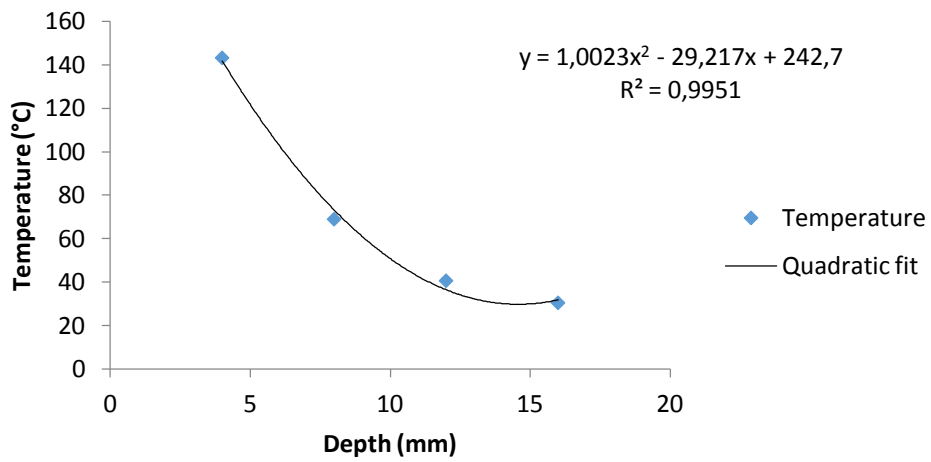
#### T-40-2-T



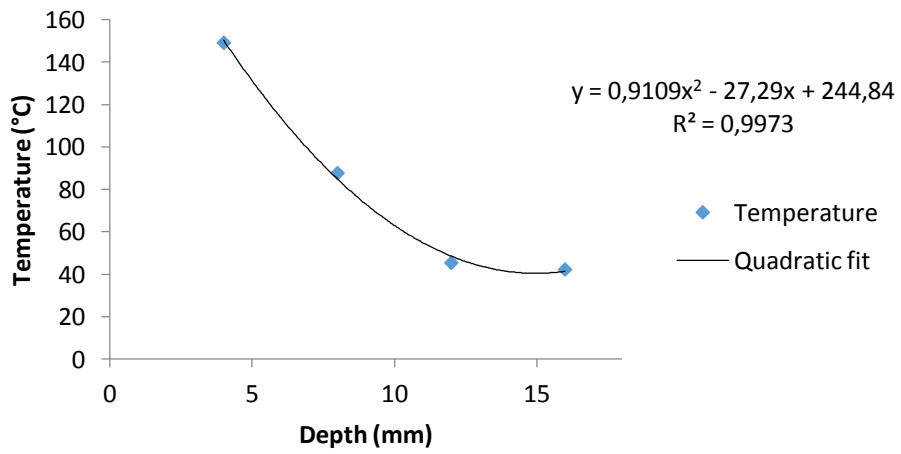
#### T-60-1-T



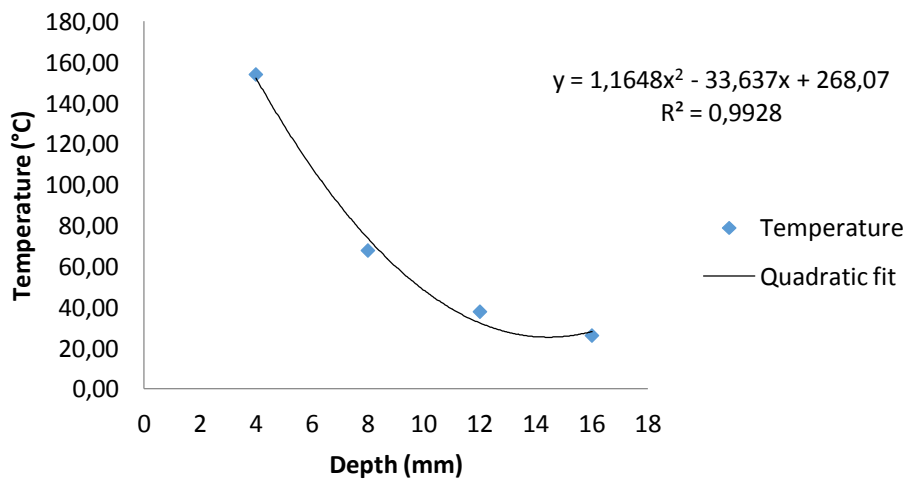
### T-60-2-T



### T-60-3-T



### T-80-1-T



### T-80-2-T

